PHYSICAL REVIEW D **89,** 072004 (2014)

A method for measuring coherent elastic neutrino-nucleus scattering at a far off-axis high-energy neutrino beam target

S. J. Brice,[1] R. L. Cooper,[2,*] F. DeJongh,[1] A. Empl,[3] L. M. Garrison,[2] A. Hime,[4] E. Hungerford,[3] T. Kobilarcik,[1]
B. Loer,[1] C. Mariani,[5] M. Mocko,[4] G. Muhrer,[4] R. Pattie,[6] Z. Pavlovic,[4] E. Ramberg,[1] K. Scholberg,[7]
R. Tayloe,[2] R. T. Thornton,[2] J. Yoo,[1] and A. Young[6]

[1]*Fermi National Accelerator Laboratory, Batavia, Illinois 60510, USA*
[2]*Indiana University, Bloomington, Indiana 47405, USA*
[3]*University of Houston, Houston, Texas 77204, USA*
[4]*Los Alamos National Laboratory, Los Alamos, New Mexico 87545, USA*
[5]*Virginia Tech, Blacksburg, Virginia 24061, USA*
[6]*North Carolina State University, North Carolina 27695, USA*
[7]*Duke University, Durham, North Carolina 27708, USA*

(Received 25 November 2013; published 3 April 2014)

We present an experimental method for measuring the process of coherent elastic neutrino-nucleus scattering (CENNS). This method uses a detector situated transverse to a high-energy neutrino beam production target. This detector would be sensitive to the low-energy neutrinos arising from decay-at-rest pions in the target. We discuss the physics motivation for making this measurement and outline the predicted backgrounds and sensitivities using this approach. We report a measurement of neutron backgrounds as found in an off-axis surface location of the Fermilab Booster Neutrino Beam (BNB) target. The results indicate that the Fermilab BNB target is a favorable location for a CENNS experiment.

DOI: 10.1103/PhysRevD.89.072004 PACS numbers: 29.25.-t, 13.15.+g, 23.40.Bw, 95.35.+d

I. INTRODUCTION

The coherent elastic neutrino-nucleus scattering process, or CENNS, has yet to be observed since its first theoretical prediction in 1974 by D. Freedman [1]. The coherence condition requires a sufficiently small momentum transfer to the target nucleus so that the waves of the off-scattered nucleons in the nucleus are all in phase and add up coherently. Neutrinos with energies less than 50 MeV largely fulfill this coherence condition in most target materials. The elastic neutral current interaction leaves no observable signature other than the low-energy recoils of the nucleus with energies of up to tens of keV. The technical difficulties of developing large-scale, low-energy threshold, and low-background detectors have hampered the experimental realization of the CENNS measurement. However, recent innovations in dark matter detector technology have made a first measurement of the CENNS possible.

Neutrinos and dark matter are similar in that they exist ubiquitously in the Universe and interact very weakly. All major direct-detection dark matter searches rely on the postulate of coherent scattering of these massive particles off of nuclei. Because of the relatively low momentum transfer, the total interaction cross section scales as the atomic mass squared of the target material. This is an analogy for low-energy neutrinos interacting coherently with nuclei. In fact, the CENNS interactions may prove to be an irreducible background for future direct-detection dark matter searches.

Besides its role as a fundamental background in dark matter searches, measurement of the CENNS process impacts a significant number of physics and astrophysics topics. These include supernova explosions, neutron form factor, sterile neutrino, neutrino magnetic moments and other non-Standard Model (SM) physics.

The method we outline uses low-energy neutrinos arising from pion decay at rest in an existing high-energy neutrino beam [2]. This differs from other methods for which detectors are proposed to be situated close to the core of a nuclear reactor [3,4] or spallation neutron sources [5,6]. The detector concept we have adopted here is similar to the CLEAR proposal [5].

In this paper, we present Research and Development for a measurement of CENNS. We start by discussing the physics motivation for the CENNS process in Sec. II. The details of the high-intensity and low-energy neutrino flux from the Fermilab Booster Neutrino Beam (BNB) are explained in Sec. III. The beam-correlated background and cosmogenic background measurements at the BNB target building are described in Sec. IV, a conceptual CENNS experiment is described in Sec. V, and we present a summary in Sec. VI.

II. PHYSICS MOTIVATION

In the Standard Model, CENNS is mediated by Z^0 vector boson exchange (see Fig. 1). In this process a neutrino of any flavor scatters off a nucleus with the same strength;

---

[*] Corresponding author.
roblcoop@indiana.edu

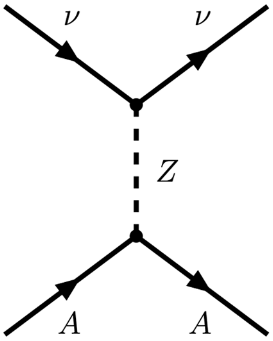

FIG. 1. Feynman diagram of the CENNS process.

hence, the measurement will be insensitive to neutrino flavor and will be blind to neutrino oscillations among the active flavors. The dominant cross section for a spin-zero nucleus at an incident neutrino energy of E_ν is given by

$$\sigma_{\nu A} \simeq \frac{4}{\pi} E_\nu^2 [Z w_p + (A - Z) w_n]^2, \tag{1}$$

where Z is an atomic number and A is an atomic mass. νA stands for neutrino-nuclei interaction. The vector charge of Z^0 to u-quark $(\frac{1}{4} - \frac{2}{3}\sin^2\theta_{\mathrm{W}})$ and Z^0 to d-quark $(-\frac{1}{4} + \frac{1}{3}\sin^2\theta_{\mathrm{W}})$, where θ_{W} is the Weinberg angle, causes the different coupling strength between w_p and w_n to the proton (uud) and the neutron (udd), respectively. The SM values are $w_p = \frac{G_F}{4}(4\sin^2\theta_{\mathrm{W}} - 1)$ and $w_n = \frac{G_F}{4}$. Since $\sin^2\theta_{\mathrm{W}} \simeq 0.23$, w_p is suppressed, and the νA cross section at a given neutrino energy is effectively proportional to the square of the number of neutrons, $(A - Z)^2$.

Typical values of the total CENNS cross section for medium-A nuclei are in the range of $\sim 10^{-39}$ cm^2 which is at least an order of magnitude larger than other neutrino interactions in this energy range (see Fig. 2). For example, charged-current inverse β decay on protons has a total cross section of $\sigma_{\bar{\nu}_e p} \simeq 10^{-40}$ cm^2, and elastic neutrino-electron scattering has a total cross section of $\sigma_{\nu_e e} \simeq 10^{-43}$ cm^2. The maximum nuclear recoil energy for a target nucleus of mass M is given by $2E_\nu^2/M$ which is in the sub-MeV range for $E_\nu \sim 50$ MeV and for typical detector materials.

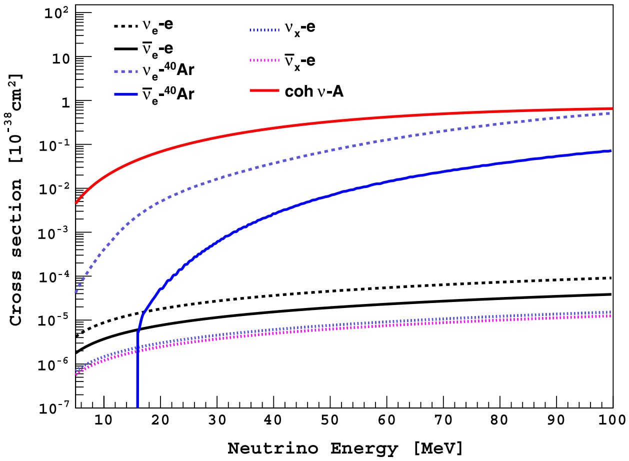

FIG. 2 (color online). Neutrino cross sections on argon target in low-energy region.

In the following subsections we briefly summarize the important physics cases where the CENNS interactions play a significant role.

A. CENNS in particle astrophysics

1. Dark matter physics

One of the most fascinating problems in particle astrophysics is the presence of dark matter. The Standard Model does not accommodate a suitable dark matter particle candidate; therefore, dark matter is crucial phenomenological evidence for physics beyond the Standard Model (BSM). The common theme of BSM scenarios is the introduction of new particles where at least one is neutral and stable. In most scenarios, these new particles typically have nongravitational interactions which are sufficient to keep them in thermal equilibrium in the early universe. In particular, particles with a mass of the electroweak scale have a relic density in the right range for a suitable candidate for dark matter.

In the limit of vanishing momentum transfer the dark matter to nuclei (χA) cross section becomes

$$\sigma_{\chi A} \simeq \frac{4}{\pi} \mu_{\chi A}^2 [Z f_p + (A - Z) f_n]^2, \tag{2}$$

where $\mu_{\chi A}$ is the reduced mass of the collision. A spin-independent χA interaction corresponds to a coupling to the nucleon density operators characterized by coupling constants f_p and f_n to protons and neutrons, respectively. In a wide range of BSM scenarios [7,8], the Higgs-to-strange quark coupling is the dominant component of the $\chi A \to \chi A$ interaction. Since the proton and neutron have similar strange quark contents, it is usually assumed that $f_p \simeq f_n$. The $\sigma_{\chi A}$ is, therefore, simplified to be proportional to A^2. This A^2 scaling of the cross section is a very strong driving force in the direct detection of dark matter experiments and is analogous to the $(A - Z)^2$ scaling in CENNS.

A recent study showed background limits to future dark matter searches coming from CENNS interactions of astrophysical and atmospheric neutrinos [9–11]. There are a few possible ways to improve the limits by using directional measurements of the neutrino interactions and/or measuring time variation of the interactions. However, this CENNS background limit is a robust lower bound which cannot be substantially reduced. Measuring the CENNS cross section and performing subsequent tests of higher energy neutrino interactions on various target materials will be extremely beneficial to future dark matter experiments. The importance of the CENNS physics cases in dark matter searches is also pointed out in a recent report [12].

2. Supernova physics

The major unsolved problem of a supernova explosion is to understand how the burst of neutrinos transfers its energy to produce the shock wave that causes the star to explode. CENNS plays a major role in an explosion of a core-collapse supernova [13]. In the core of the dying star, neutrinos are scattered, absorbed, and reemitted by superdense proton-neutron matter. Although yet to be fully understood, modern numerical simulations show that neutrino-driven convection eventually causes the giant star to explode. A CENNS cross section different from the nominal SM prediction could have significant impact on the understanding of supernova explosions.

Moreover, CENNS is an important process for the detection of supernova neutrinos. Future large-scale, low-energy threshold, underground detectors, such as the CLEAN detector [14–16], will be sensitive to all active neutrino species in a supernova burst and will be flavor blind [17]. Hence, detecting supernova neutrinos in such a detector may provide a total flux and spectrum of neutrinos from supernova if the cross section of CENNS can be independently and accurately measured. These results combined with flavor-dependent interaction measurements [18,19] can explain how neutrinos are thermalized with matter in a supernova.

B. CENNS in particle physics

1. Neutrino oscillations

Neutrino flavor oscillation is a well-established physics phenomenon studied over the last four decades. Neutrino disappearance and appearance signatures are successfully explained by representing the neutrino flavor eigenstates as a mixture of nonzero mass eigenstates. There has been huge progress in measuring neutrino mixing angles during the last decades. Identifying mass hierarchies, measuring *CP* phase(s) and determining whether neutrinos are Dirac or Majorana particles are active topics in the field. CENNS is a large and well-predicted cross section in the Standard Model. If discovered at its predicted rate, the CENNS process can become a powerful tool for future low-energy neutrino physics, especially for neutrino oscillation experiments.

A number of recent anomalous results suggest the existence of a sterile neutrino [20,21]. In these experiments, an excessive appearance of active-flavor neutrinos is seen. If confirmed, this excess requires a model which has relatively large mass differences ($\Delta m^2 \sim 1\ \text{eV}^2$) and requires at least one more mass eigenstate (m_4) in the neutrino mass spectrum. Most of the previous experiments are based on charged-current measurements, and hence are indirectly inferring the mixing matrix elements. However, the sterile neutrino models can be clearly verified by CENNS interactions. The CENNS interaction is insensitive to the differences of active flavors of neutrinos, thus the measurement will be of total fluxes of active-flavor neutrinos. Sterile neutrino oscillations manifest themselves as a baseline- and energy-dependent disappearance of CENNS interactions. A short-baseline neutrino experiment measuring CENNS has the potential to probe a wide range of oscillation hypotheses [22,23].

A sensitivity study of a future sterile neutrino search using CENNS has been carried out in reference [23]. The study assumes neutrino fluxes of $2.5\times10^7 (6.3\times10^6)\nu/\text{cm}^2/\ \text{sec}$ per flavor at 20 m (40 m) from the pion decay-at-rest neutrino source with one near (20 m) detector with 456 kg of liquid argon and four far (40 m) detectors. With this experimental scenario, one can test the LSND best-fit mass splitting ($\Delta m^2 = 1.2\ \text{eV}^2$) at the 3.4 sigma significance.

2. Neutrino magnetic moment

As a consequence of nonzero masses, neutrinos can have magnetic moments. In the minimally extended SM, Dirac neutrinos of mass m_ν have a magnetic moment through one-loop radiative corrections [24]. The magnetic moment is given by

$$\mu_\nu = \frac{3G_F m_e m_\nu}{4\pi^2\sqrt{2}}\mu_B \simeq 3.2\times10^{-19}\left(\frac{m_\nu}{1\ \text{eV}}\right)\mu_B, \qquad (3)$$

where G_F is the Fermi constant, m_e is the electron mass, and $\mu_B (= e/2m_e)$ is Bohr magnetons. This predicted value in an extended SM is too exceedingly small to be measured. However, beyond the SM models commonly predict larger values of μ_ν, and hence any measurement of excessive neutrino magnetic moment would be a signature of BSM physics [25]. There are several consequences of the neutrinos having large magnetic moments. The neutrino-electron scattering cross section would be modified in low energies. Neutrinos would flip their spin in strong external magnetic fields which is, for example, a natural configuration for the core region of stars. Heavier-mass neutrinos would decay radiatively to lighter-mass neutrinos and emit photons.

The best direct experimental limit for a neutrino magnetic moment comes from the measurement of $\nu - e$ scattering in the GEMMA experiment, $\mu_\nu(\bar{\nu}_e) \le 0.32\times10^{-10}\mu_B$ [26]. For muon neutrino scattering, the best limit is less stringent: $\mu_\nu(\nu_\mu) \le 6.8\times10^{-10}\mu_B$ [27]. The most stringent limits are from astrophysical observations with several assumptions. For example, a model-dependent analysis of plasmon decay in red giant evolution [28] and an analysis of neutrino spin-flip precession in Supernova 1987 A set limits of $\mu_\nu \le 10^{-12}\mu_B$ [29].

A finite neutrino magnetic moment can be observed in the recoil spectrum of CENNS. The magnetic scattering cross section is given by [24],

$$\left(\frac{d\sigma}{dE_R}\right)_m = \frac{\pi\alpha^2\mu_\nu^2 Z^2}{m_e^2}\left(\frac{1 - E_R/E_\nu}{E_\nu} + \frac{E_R}{4E_\nu^2}\right), \qquad (4)$$

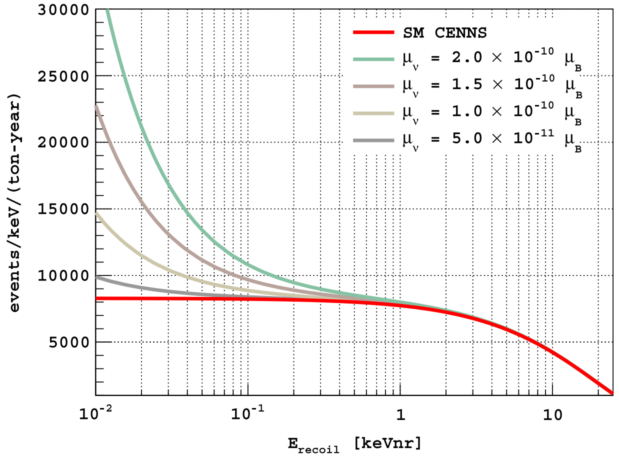

FIG. 3 (color online). Differential yield as a function of nuclear recoil energy for different values of neutrino magnetic moment ($\mu_\nu(\nu_\mu)$). ν_μ flux of 2.5×10^7 $\nu/\mathrm{cm}^2/\mathrm{s}$ from pion decay-at-rest source is assumed.

where α is the fine structure constant and E_R is the recoil energy of nuclei. Figure 3 shows the event rates as a function of energy thresholds in a germanium detector with pion decay-at-rest ν_μ flux of 2.5×10^7 $\nu/\mathrm{cm}^2/\mathrm{s}$ for various magnetic moment contributions. Future detectors for sub-keV recoil energy thresholds would begin to directly test new regimes of neutrino magnetic moment.

3. *Non-Standard Model interactions*

The CENNS cross section is well predicted in the SM. Therefore, any deviation from the predicted value would be an indication of BSM physics. Any nonstandard interactions (NSI) which are specific to the interactions of neutrinos and quarks can be parameterized in a relatively model-independent way. An effective Lagrangian of a neutrino with a hadron in the parametrization of ε_{ij} can be described as [30,31]

$$\mathcal{L}^{\mathrm{NSI}}_{\nu H} = -\frac{G_F}{\sqrt{2}} \sum_{\substack{q=u,d \\ \alpha,\beta=e,\mu,\tau}} [\bar{\nu}_\alpha \gamma^\mu (1-\gamma^5)\nu_\beta] \times (\varepsilon^{qL}_{\alpha\beta}[\bar{q}\gamma_\mu(1-\gamma^5)q] + \varepsilon^{qR}_{\alpha\beta}[\bar{q}\gamma_\mu(1+\gamma^5)q]), \tag{5}$$

where α and β are the index of neutrino flavors, q is the index of up or down quark, L or R is the left- or right-handedness respectively, and the ε parameters represent either nonuniversal ($\alpha = \beta$) or flavor-changing ($\alpha \neq \beta$) interactions. Many of these parameters are quite poorly constrained, and CENNS experiments can improve sensitivity by an order of magnitude [30,32,33]. The cross section for CENNS of ν_α off a spin-zero nucleus (A) is given by

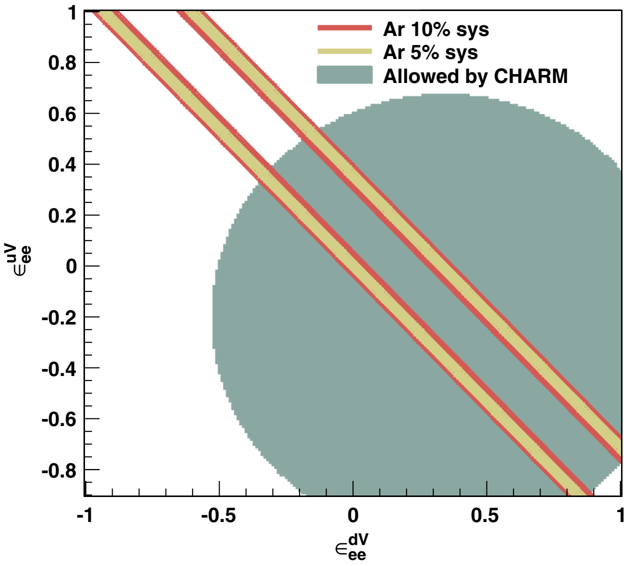

FIG. 4 (color online). Allowed regions (red and yellow shaded areas) at 90% C.L. assuming measurement of the SM-predicted CENNS rate, for ϵ^{uV}_{ee} and ϵ^{dV}_{ee} for 1 ton-year liquid argon detector at 5×10^6 $\nu/\mathrm{cm}^2/\mathrm{s}$ per flavor of pion decay-at-rest neutrino flux, assuming 5% or 10% of systematic uncertainty in measurement. The energy threshold is assumed at 25 keV_{nr} (nuclear recoil). The shaded elliptical region corresponds to a slice of the CHARM-experiment-allowed NSI parameter space, for $\epsilon^{qA}_{ee} = 0$.

$$\left(\frac{d\sigma}{dE}\right)_{\nu_\alpha A} = \frac{G_F^2 M}{\pi} F^2(2\,\mathrm{ME}) \left[1 - \frac{ME}{2k^2}\right] \times \{[Z(g^p_V + 2\varepsilon^{uV}_{\alpha\alpha} + \varepsilon^{dV}_{\alpha\alpha}) + N(g^n_V + \varepsilon^{uV}_{\alpha\alpha} + 2\varepsilon^{dV}_{\alpha\alpha})]^2 + \sum_{\alpha\neq\beta}[Z(2\varepsilon^{uV}_{\alpha\beta} + \varepsilon^{dV}_{\alpha\beta}) + N(\varepsilon^{uV}_{\alpha\beta} + 2\varepsilon^{dV}_{\alpha\beta})]^2\},$$

where $g^p_V = (\frac{1}{2} - 2\sin^2\theta_W)$, $g^n_V = -\frac{1}{2}$ are the SM weak constants. Figure 4 shows allowed regions for ϵ^{uV}_{ee} and ϵ^{dV}_{ee}, for 1 ton-year of liquid argon detector data assuming high-intensity pion decay-at-rest neutrino flux. The shaded elliptical region corresponds to constraints by the CHARM experiment [34]. Hence, a CENNS experiment at an intense stopped-pion neutrino source would have significant sensitivity to currently allowed NSI interaction parameters.

C. CENNS in nuclear physics

Determination of the neutron distributions in nuclei is important not only for fundamental understanding of nuclear physics, but also because of important implications for astrophysics. For example, the primary physics quantities of neutron stars such as masses, radii, and composition are determined using the equations of state of neutron-rich nuclei. The equation of state is related to the nuclear symmetry energy, which is defined as $E(n,\delta) \simeq E_0(n) + E_{\mathrm{sym}}\delta^2$ and $\delta = (n_n - n_p)/(n_n + n_p)$, where n_n and n_p are the number densities of neutrons and protons. The symmetry energy is strongly correlated with the skin thickness of neutrons [35], and hence the radii of neutrons. Therefore, the size of neutron stars can be predicted more precisely based on better measurements of the equation of state. Traditional methods of measuring neutron radii through hadronic scattering report typical uncertainties of order 10% [36].

The CENNS interaction is especially sensitive to neutron numbers in target nuclei, which provides a clean way to measure the neutron part of nuclear form factors. At low momentum transfer, the form factor $F(Q^2) \sim 1$. However for higher Q values, small deviations from coherence occur as higher-order terms of the nuclear form factors come into play [37]. The CENNS cross section of the spin-zero nucleus is given by

$$\left(\frac{d\sigma}{dE}\right)_{\nu A} = \frac{G_F^2}{2\pi}\frac{Q_w^2}{4}F^2(Q^2)M\left[2 - \frac{ME_R}{E_\nu^2}\right], \tag{6}$$

where M is the nuclear mass, Q_w is the weak charge, and $Q = \sqrt{2ME_R}$. The form factor $F(Q^2)$ can be expanded as

$$F_n(Q^2) \sim N\left(1 - \frac{Q^2}{3!}\langle R_n^2\rangle + \frac{Q^4}{5!}\langle R_n^4\rangle + \cdots\right), \tag{7}$$

where $\langle R_n^i\rangle$ are the even moments of the neutron density. Such deviations are observable as small distortions of the expected recoil spectral shape and can be exploited to measure nucleon density distributions. With good control of spectral shape uncertainties, multi-ton-scale experiments could make meaningful measurements of the neutron radius $\langle R_n^2\rangle^{1/2}$ and potentially higher-order moments.

According to Ref. [36], a exposure of 3.5 ton-year with a liquid argon detector with neutrino flux of $3 \times 10^7\ \nu/\mathrm{cm}^2/\mathrm{s}$ per flavor is required to measure the second and fourth moments of the form factor. The experimental requirements are challenging to reach in the near future; however, it is possible to determine the neutron radius to a few percent by measuring neutron form factor with sufficient accuracy. The precise measurements of neutron radii then improve the predictive power of the equation of state of neutron matter, and thus the knowledge of the size of neutron stars [35,38].

D. Summary

In order to achieve the above physics goals, a phased approach is most appropriate, depending on the available neutrino beam power and detector technology.

(1) The first-generation CENNS experiment would be the discovery of the CENNS interaction and measurement of the cross section with ~10% accuracy. The experiment can be carried out with existing dark matter detector technology in an existing beamline and target station—for instance at Fermilab, as discussed below. The result would be sensitive to the NSI ranges as well.

(2) The second-generation experiment would be the precision measurement of the CENNS cross section. The accurate measurement of the neutrino flux, assuming the cross section is exactly known, would be a powerful tool for neutrino oscillation studies [39] and future low-energy neutrino experiments. This would also allow an initial series of measurements of supernova-related neutrino cross sections on a variety of targets [40], many of which have not been measured. The precision measurement of the CENNS cross section will be a valuable input to the next generation of dark matter experiments.

(3) The third-generation CENNS experiment would use a high-intensity neutrino beam and large-scale neutrino detector with a lower energy threshold. The goal would be a search for the neutrino magnetic moment, measurement of the neutron form factor, and possible deviations of the SM.

The major focus in this paper is the first-generation of CENNS experiment—the discovery of the CENNS. There are a few existing intense, pion decay-at-rest sources: for example, the Spallation Neutron Source at Oak Ridge National Laboratory [41]. In this paper, we present a promising alternative setup at an existing neutrino beam at Fermilab. The unique idea presented here uses the low-energy neutrinos produced at a far off-axis location from the neutrino target [2].

III. LOW-ENERGY NEUTRINO SOURCE AT FERMILAB

Fermilab has two major neutrino beam lines (see Fig. 5): the Neutrinos at the Main Injector (NuMI) and the Booster Neutrino Beam (BNB). The energy range of these two neutrino sources on axis is in the GeV range, which is too high to satisfy the condition for dominance of coherent scattering. We found the far off axis (>45 degrees) of the BNB produces well-defined neutrinos with energies below ~50 MeV. The BNB source has substantial advantages over the NuMI beam source owing to suppressed kaon production from the relatively low-energy 8 GeV proton beam on the target. Therefore, pion decay and subsequent muon decay processes are the dominant sources of neutrinos. At the far off-axis area, the detector can be placed close enough to the target to gain a large increase in neutrino flux due to the larger solid angle acceptance. An initial study using the existing BNB Monte Carlo (BNB MC) has confirmed that this approach is promising.

The Fermilab Booster is a 474 m circumference synchrotron operating at 15 Hz. Protons from the Fermilab LINAC are injected at 400 MeV and accelerated to 8 GeV kinetic energy. The structure of the beam is a series of 81 proton bunches each with a 2 ns width and 19 ns apart. The maximum average repetition rate for proton delivery to the BNB target is 5 Hz and 5×10^{12} protons per pulse. The repetition limit is set by the horn design and its power

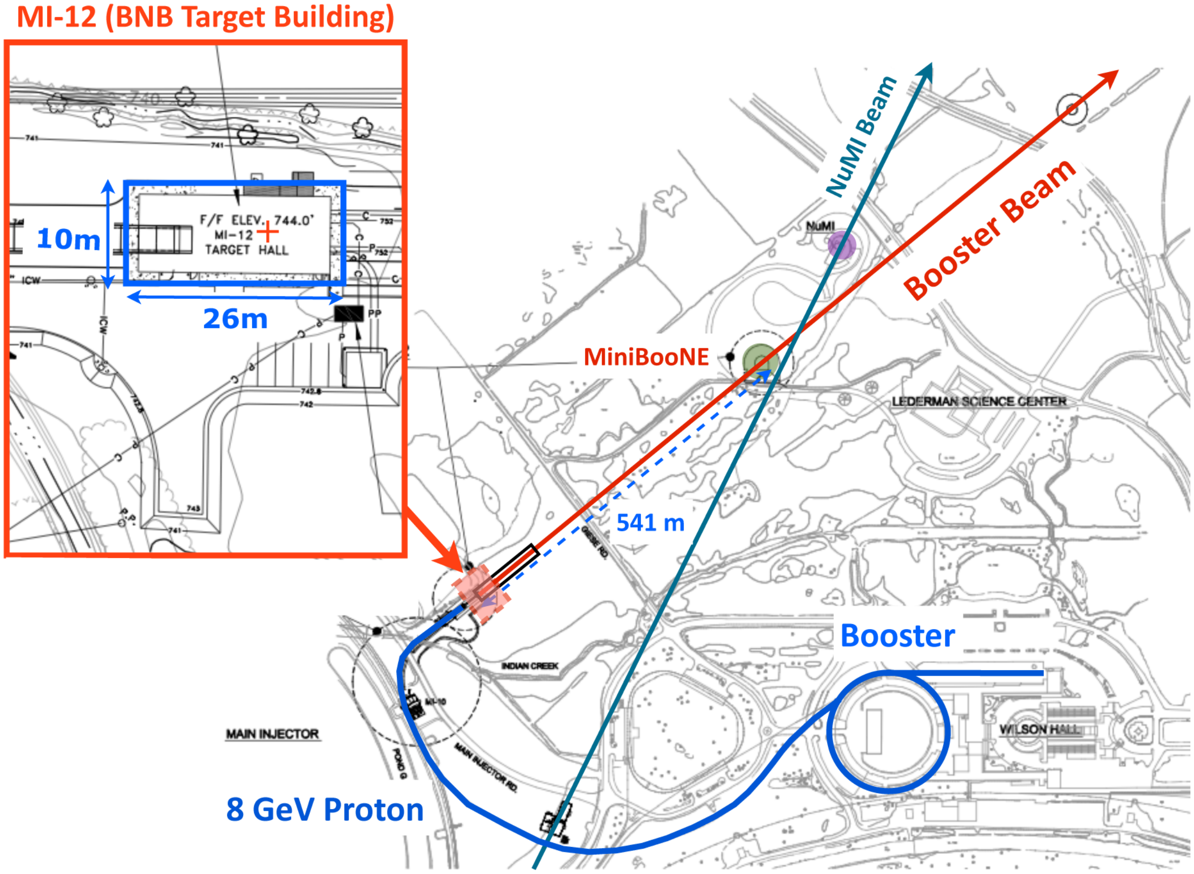

FIG. 5 (color online). Fermilab neutrino beam lines: the Booster Neutrino Beam (BNB, red line) and Neutrinos at the Main Injector beam (NuMI, green line) [42]. The left inset figure shows the configuration around BNB target building (MI-12) area [43]. The red cross in the figure indicates the location of the target. No facility equipment occupies the area near the potential experiment site.

supply. The target is made of beryllium divided in seven cylindrical sections in a total of 71.1 cm in length and 0.51 cm in radius. In order to minimize upstream proton interactions, the vacuum of the beam pipe extends to about 152 cm upstream of the target. The horn is an aluminum alloy toroidal electromagnet with operating values of 174 kA and maximum field value of 1.5 Tesla. A concrete collimator is located downstream of the target and guides the beam into the decay region. The air-filled cylindrical decay region extends for 45 m. The beam stop is made of steel and concrete. Details of the Fermilab BNB neutrino fluxes can be found in [44].

At very far off axis, the pion decay region is no longer a point source, and the angle from on axis is not a well-defined quantity. Moreover, the geometry around the target area and shielding should be properly taken into account in the neutrino flux calculation, as the secondary hadronic processes in the shielding material also produce pions and hence neutrinos. In particular, the pion production from the 8 GeV BNB proton beam on the beryllium target, the multiplicity of pion production from the subsequent π-p interactions, and defocused π^-s from the horn all require a well-modeled MC study.

In order to understand the neutrino flux at BNB far off axis, we adapted the BNB MC. The BNB MC uses the Geant-4 framework for propagating particles, for electromagnetic processes, hadronic interactions in the beamline materials, and the decay of particles. The geometry of the target area and beam line is accurately modeled. The double differential cross sections of pion and kaon production in the simulation have been tuned to match external measurements. This is true for the hadronic cross sections for nucleons and pions as well [44]. The original BNB MC, however, contains a hard-coded tracking threshold cut to remove stopping pions (defined as below 1 MeV in kinetic energy). In fact, the stopping pions are the dominant neutrino source at far off axis. The cut does not affect any previous on-axis BNB experiments such as MiniBooNE and SciBooNE which focus on above 100-MeV neutrino interactions.

The BNB MC simulation was carried out in neutrino mode with 173 kA horn current and 8 GeV proton momentum. Figure 6(a) shows the angular distribution of the neutrino flux 20 m away from a reference point of the upstream end of the decay pipe where the angle is measured from on axis. The flux of the neutrinos, at the 32 kW

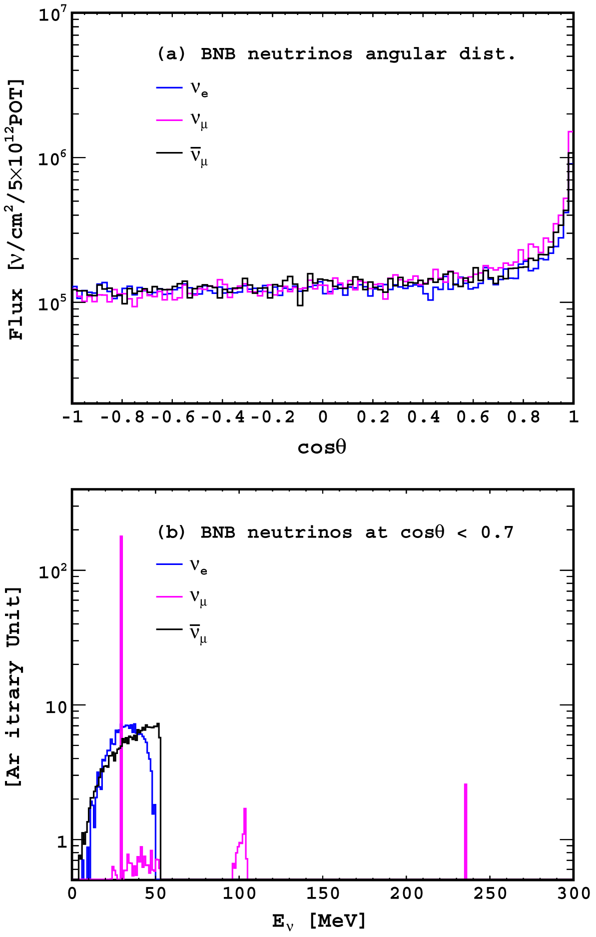

FIG. 6 (color online). Estimated neutrino flux from modified BNB MC in ν mode, 173 kA horn current and 8 GeV BNB configuration. The neutrino flux is normalized per 5×10^{12} protons on target. (a) The angular dependence of the neutrino fluxes for different flavors. The flux becomes uniform below $\cos\theta < 0.7$. See text for the definition of θ. (b) Energy spectrum of neutrinos below $\cos\theta < 0.7$ (far off axis) for different flavors.

maximum BNB power [5×10^{12} protons on target (POT) per pulse], is estimated to be about 10^5 ν/cm^2/pulse per flavor with 5 Hz frequency within a pulse width of 1.6 μs. Hence, the neutrino flux per unit time is about 5×10^5 $\nu/\text{cm}^2/\text{s}$. Figure 6(b) shows the energy spectrum of neutrinos at angles less than $\cos\theta < 0.7$ which is dominated by neutrinos from stopping pion decay. The pion decay at rest ($\pi^+ \to \mu^+ \nu_\mu$) produces a prompt and monochromatic ν_μ at 29.9 MeV. The μ^+ then decays with a 2.2 μs lifetime to produce a $\bar{\nu}_\mu$ and a ν_e with energies between 0 and $m_\mu/2$. In Fig. 6(b), the ν_μ, ν_e and $\bar{\nu}_\mu$ spectra follow the stopping π^+ decay kinematics. The small ν_μ bump at ~100 MeV is due to the neutrinos from μ^- capture on nuclei. The peak at 235.3 MeV is from kaon decay at rest. These ν_μs above 55 MeV are potential background sources since the interaction of neutrinos may scatter off neutrons from nuclei nearby or inside the detector.

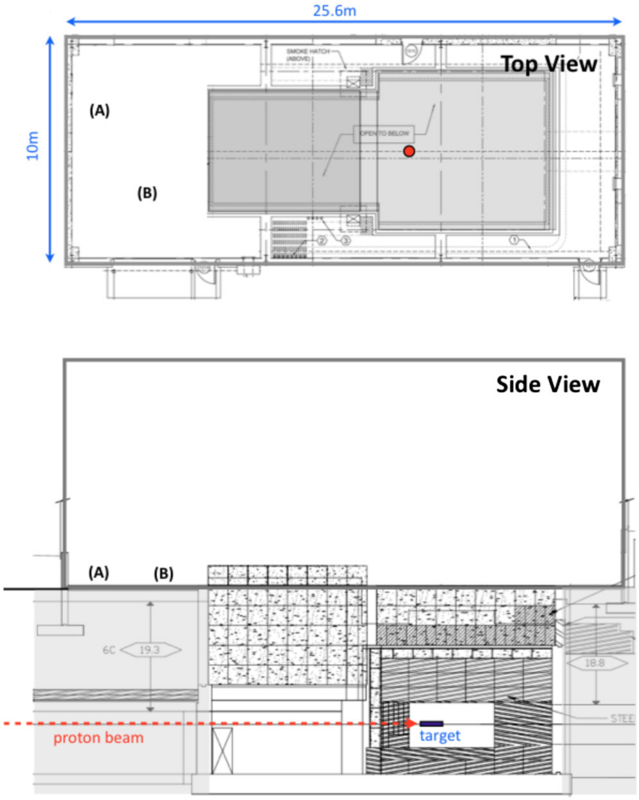

FIG. 7 (color online). The top-down and elevation views of the BNB target building. The SciBath detector was operated at location (A) and the EJ-301 measurement carried out at location (B). The drawing is taken from [43] and modified. The red-filled circle in the top figure indicates the upstream end of the target position.

The existing radioactive shielding at the BNB target area is extensive and designed to satisfy the Fermilab radioactive safety regulations [45] (see Fig. 7). The target itself is located ~7 m underground from the building surface. The shielding pile consists of iron blocks totaling 2.6 m in elevation (1600 tons), an additional 3.2 m thick concrete shielding (300 tons), and special custom sized steel (40 tons) above and below the horn module. About 3×10^{22} neutrons per 10^{21} POT (year) are expected to be initially produced at the target. These neutrons are produced in the forward beam direction with a maximum kinetic energy of ~8 GeV with more than 90% of neutrons below 50 MeV. The high-energy neutrons scatter off the surrounding materials and produce secondaries. Considering the existing shielding configuration, the beam-induced neutron flux at about 20 m away from the target is roughly estimated to be ~3.6×10^8 neutrons/m^2 per 10^{21} POT. According to a simple linear scaling of neutron shielding, an additional ~8 m thick concrete barrier would be enough to shield out most of the beam-induced neutrons. Although the estimated beam-induced neutron background is sufficiently low, it is also true that predicting neutron leakage rates through massive shielding material is notoriously difficult. For example, a small gap between shielding blocks may potentially cause serious leakage of neutron fluxes. Any fast neutron backgrounds would require a more extensive study for the shielding design. Therefore, measuring the beam coincident neutron flux and energy spectrum at the experimental site is necessary. With the help of the Fermilab Accelerator Division, we carried out beam-induced background studies at the BNB target building, which is described in Sec. IV.

The far off-axis site of the BNB is also the far off-axis site of the NuMI beam (see Fig. 5). The NuMI beam contains a potential source of background from high-energy neutrinos (> 200 MeV) from kaon decay. However, the distance from the NuMI target to the BNB far off-axis site is more than 200 m away, and the NuMI neutrinos can be vetoed out using beam trigger information. Therefore, the neutrinos from the NuMI beam line should be significantly suppressed.

Beam-uncorrelated backgrounds are mitigated by the BNB beam window; the timing allows a factor of 5×10^{-5} rejection ("duty factor," hereafter) of steady-state backgrounds assuming a 10 μs detector time window. The total detector beam-on livetime per year is only ~26 min ($= 5 \times 10^{-5} \times$ year). Timing of individual events in the detector can be known to within ~10 ns using detectors with fast timing. Furthermore, these backgrounds can be subtracted using beam-off data. Cosmic ray–related backgrounds will be significantly reduced by the water shielding veto system.

IV. NEUTRON BACKGROUNDS MEASUREMENT

A commercial EJ-301 liquid scintillator neutron detector and a newly developed neutral particle detector, named SciBath [46,47], were used to measure the neutron backgrounds in the BNB target building.

A. EJ-301 liquid scintillator

To obtain a rough estimate of the neutron background from the BNB, we attempted to measure the neutron flux with a commercial liquid scintillator detector [Eljen 510-50x50-1/301 liquid scintillation detector assembly, a sealed system with 5" ETEL-9390KB PMT (photomultiplier tube) and EJ301 scintillator]. The PMT signals were recorded from 3 μs before to 20 μs following the beam trigger using a CAEN V1720 250 MS/s, 12-bit, 2 Vpp digitizer. The scintillation response of the cell to gammas of various energies was calibrated using the Compton edges of ^{133}Ba, ^{137}Cs, and ^{22}Na sources, from which the energy of proton recoils can be obtained using Table 1 of reference [48]. (The scintillation light output for 1 MeV proton recoils is quenched by a factor ~0.16 relative to electrons.) Given the gain of the phototube, pulses begin to exceed the vertical range of the digitizer at around 500 p.e. (photoelectron) for gamma events (~700 p.e. for neutron events due to the slower scintillation pulses). We have measured beam-induced events with energies up to 8000 p.e., or > 4 MeVee, but we have not calibrated the effect of the digitizer saturation in order to correct the energy scale at these energies.

Discrimination between electron recoil (gamma-induced) and nuclear recoil (neutron-induced) events can be achieved via pulse shape discrimination (PSD) [49,50]. We have adopted F90, the fraction of photons collected in the first 90 ns of a scintillation pulse, as our PSD variable. Figure 8 shows F90 as a function of energy for ^{252}Cf and ^{22}Na sources. Based on this calibration, neutron events will have F90 in the range 0.76–0.91, while gammas have faster pulses with $F90 > 0.91$. (Calculated values of $F90 > 1$ may occur due to not accounting for baseline drift in our analysis.) Discrimination with the PSD parameter degrades rapidly at low energies due to the limited photon statistics. PSD also fails in the high-energy region above the digitizer saturation point, as described above. For this reason, we restrict the neutron analysis to the region between 50 and 700 p.e., which corresponds to approximately 0.3 to 1.6 MeV imparted to the recoiling proton.

Figure 9 (top) shows the F90 parameter vs detection time for events in the 50–700 p.e. range. The tail of events with $F90 < 0.75$ is most likely due to pileup events. The 1.7 μs beam spill is evident in the region from −0.6 to 1.1 μs on this time scale, and the events in this region are overwhelmingly gammalike; after the spill, the rate is dominated by neutronlike events. The rate of neutronlike events peaks partway through the beam spill, then decays away with a characteristic time of a few μs. Figure 9 (bottom) shows the event energy as a function of time, from which it is clear that the energy of the neutronlike events also decays with the same few μs timescale. Both of these observations

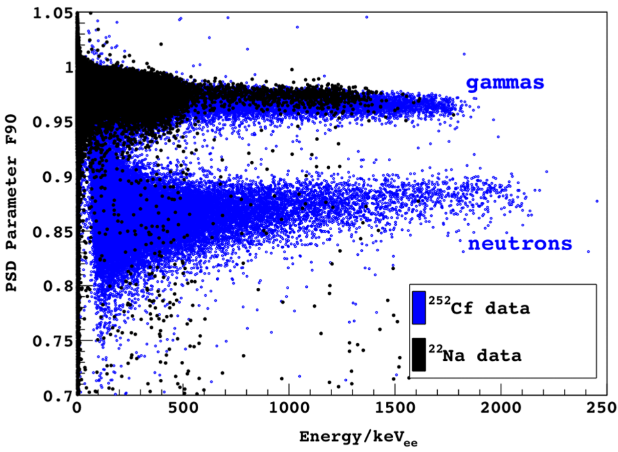

FIG. 8 (color online). Calibration of the energy and pulse shape discrimination parameter F90 for the EJ301 scintillator detector with neutron (^{252}Cf) and gamma (^{22}Na) sources. Neutrons are defined as events having F90 between 0.76 and 0.91 and energy below the digitizer saturation point (around 2 MeV$_{ee}$, electron equivalent energy, on this scale; saturating events are excluded from this plot) and above the point where the gamma and neutron F90 distributions merge (around 200 keV$_{ee}$ on this scale).

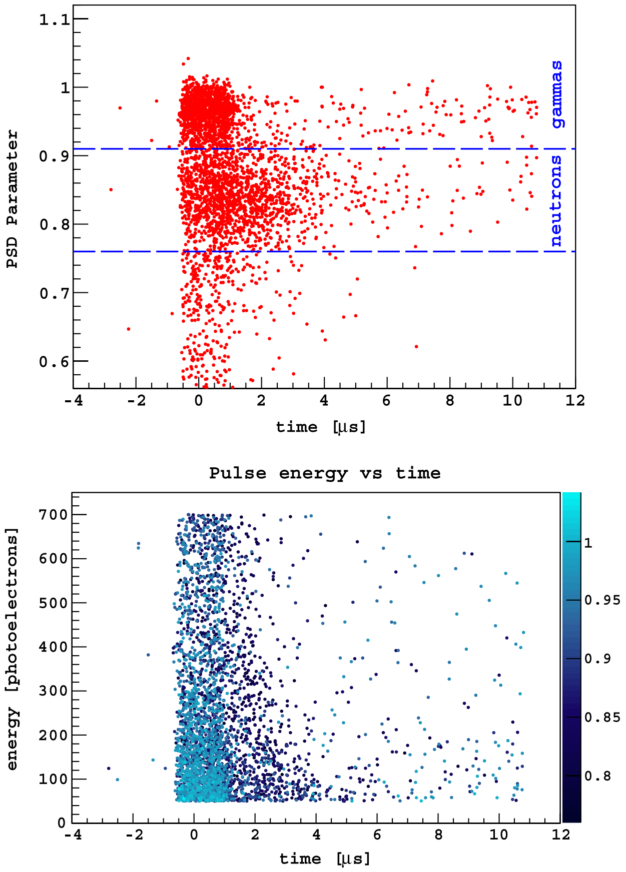

FIG. 9 (color online). Top: Pulse shape discrimination parameter of scintillation events in the EJ301 detector vs time relative to the beam trigger. Bottom: Energy of scintillation pulses measured in the 5” EJ301 detector vs time. The color scale for each point shows the PSD parameter, with darker colors being more neutronlike.

are roughly what one would expect from neutrons gradually losing energy to elastic scattering in the shielding material and the building.

Although this measurement lacked precise calibration and required a small analysis window, with this first look we were able to determine the overall scale of the neutron background. Very few cuts were placed on the analysis, but those that were applied should have had the effect only of rejecting nuclear-recoil events while admitting a minimal amount of electron-recoil events. The measured rate of recoil-like events in the 0.3–1.6 MeV range (assuming protons) in the liquid scintillator detector is ~0.09 events per beam trigger. The average neutron-proton elastic scattering cross section in this energy range is approximately 6 barns, which, given the 1.4 kg total scintillator mass, gives an average flux of $> 2 \times 10^{-4}/\mathrm{cm}^2/\mathrm{pulse}$ ($\mathrm{pulse} \simeq 4.5 \times 10^{12}$ POT) neutrons with energy above 0.3 MeV at 19 m from the target. A more in-depth characterization of the beam-induced neutron flux requires a detector with larger mass, more dynamic range, and better particle discrimination, such as the SciBath detector.

B. SciBath detector

The SciBath detector is a prototype for the proposed FINeSSE detector which is a 13-ton, fine-grained, liquid scintillator neutrino tracking detector [51]. While the detection concept was originally optimized to be a fine-grained neutrino tracker, it is also an excellent neutron detector. Below, we show results from a two-month measurement of the beam-correlated neutron flux (10–200 MeV) at the BNB target building. The SciBath detector will be described briefly here. More details about the SciBath detector will appear in a future publication.

1. Detector description

The SciBath detector is an 82 L, optically-open bath of mineral oil–based liquid scintillator that serves as both an active target and scintillator. Scintillation light is produced by the recoiling charged particles from neutral particle collisions with the mineral oil or by incoming charged particles from outside the detector. This scintillation light is absorbed by a square 16 × 16 array of wavelength shifting (WLS) fibers, oriented along each detector axis, with a spacing of 2.5 cm (i.e. 768 total fibers). The light entering each fiber is Stokes-shifted and reemitted isotropically. Some of the wavelength-shifted light is then transported by total internal reflection to a multianode photomultiplier tube, where it is read out and digitized by the DAQ. The fibers shift the ultraviolet bulk scintillation light to blue where it more effectively couples to the PMT quantum efficiency peak. A schematic of the detector is shown in Fig. 10.

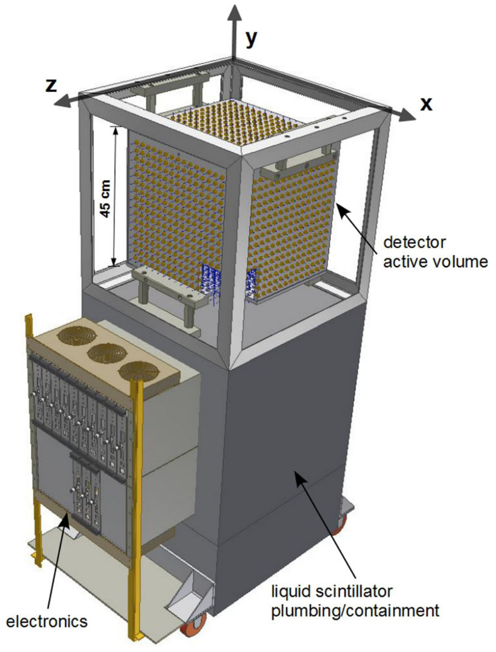

FIG. 10 (color online). A schematic drawing of the SciBath detector with its $(45\ \mathrm{cm})^3$ active volume indicated along with the other major components.

The liquid scintillator has a base of mineral oil combined with 15% pseudocumene (1,2,4-trimethylbenzene, C_9H_{12}) by volume and 1.5 g/L PPO (2,5-diphenyloxazole, $C_{15}H_{11}NO$). The mixture was created for this detector and was continuously purged with N_2. It is very similar in composition to commercially available liquid scintillators EJ-321L [52] and BC-517H [53], but it lacks tertiary wavelength shifters such as bis-MSB or POPOP. The scintillator emission peaks at approximately 370 nm, and the attenuation length for this light is over 1 m in the detector and is adequate for the WLS fiber spacing. The 1.5 mm diameter WLS fibers have an absorption peak at 345 nm, and reemission peaks at 435 nm which matches the peak quantum efficiency of the PMT. Approximately 8% of this reemitted light in the WLS fiber is collected at the PMT.

The SciBath optical properties were calibrated with cosmic ray muons and a LED pulser system. A minimum ionizing muon will deposit approximately 65 MeV into the SciBath detector and this yields approximately 400 detected p.e. The light output to energy deposit is 6 p.e./MeV, and we found this calibration to be stable to within 5% over the entire two-month run. Birks' law is used to model quenching effects for large dE/dx particles (e.g. protons). The Birks' law coefficient kB used in the Monte Carlo simulation is $0.013\ \mathrm{g\,cm^{-2}\,MeV^{-1}}$ while KamLAND reports $0.0092 \pm 0.0001\ \mathrm{g\,cm^{-2}\,MeV^{-1}}$ for the commercially similar BC-517H [54]. A pulsed LED system was coupled to the opposite end, with respect to the PMT, of each WLS fiber. Low-light LED pulses were used to measure the single p.e. response of the PMTs and calibrate the SciBath DAQ. These LED calibrations were performed every three weeks, and the gains were stable to within 10% throughout the entire run. In fact, they were stable when compared to a previous deployment six months prior.

Each PMT is mounted to a custom "integrated readout module" (IRM) which serves as both a digitizing readout and physical mounting for the PMT. They are built on a VME form factor, but they are externally powered and connectivity is established through 1-gigabit ethernet (in lieu of the VME power and connectivity standard). The front-end electronics of the IRM shapes and stretches the incoming pulses to enable simultaneous nanosecond timing resolution and spectroscopy with 20 MS/s, 12-bit flash Analog to Digital Converters. Additional processing with onboard Field-Programmable Gate Arrays and an ARM-9 microcontroller digitize and transfer 64 PMT channels simultaneously. For data collection, the DAQ was externally triggered on the beam for 20 ms with a 1/3 p.e. threshold per channel and 100 μs of pretrigger data. The LED calibration runs were also externally triggered, but only recorded 1 μs of data with no zero-suppressing threshold.

To exploit the tracking capabilities of 768 WLS fibers for a large number of events, fast algorithms were developed to determine the tracklike properties of each event. The first four statistical moments of the WLS fiber light output are calculated for each axis. A principal component analysis is then performed, giving characteristic eigenvalues and eigenvectors of the fiber hit distribution. Point-and tracklike objects can be discriminated by their characteristic eigenvalue spectra. Additionally, a pair of likelihoods are created to further discriminate point- and tracklike events. In this analysis, event topology is not used to construct the beam-correlated neutron spectrum, but it is used as a quality cut to select tracklike events for the direction spectrum.

2. Results

The SciBath detector was placed about 20 m away from the BNB target at nearly 180° with respect to the beam direction, and the detector position is shown schematically in Fig. 7. SciBath recorded ten-minute beam-on data runs starting on February 29, 2012 and ending on May 3, 2012 with a 95% total livetime. After the BNB shut down on April 23, 2012, various calibrations were performed. During the entire run, 4.90×10^{19} protons on target were delivered to the BNB target. Approximately 5.5 weeks of production-quality data are used in the analysis below, and this data set contains 3.50×10^{19} POT. The remainder of the time was used for LED calibrations and other systematic checks. A total of 2.5 TB of data was collected, with the majority of events having low fiber multiplicity (< 5); these were unused in the analysis.

Figure 11 shows the distribution of events in time around the beam window for various p.e. subgroups. The black trace with the highest count rate is all events with p.e. > 20. The red-colored trace is the group of events with $60 <$ p.e. < 200 that has an excess of events above background for a few μs after the beam pulse, after which the count rate returns to prebeam, background levels. This

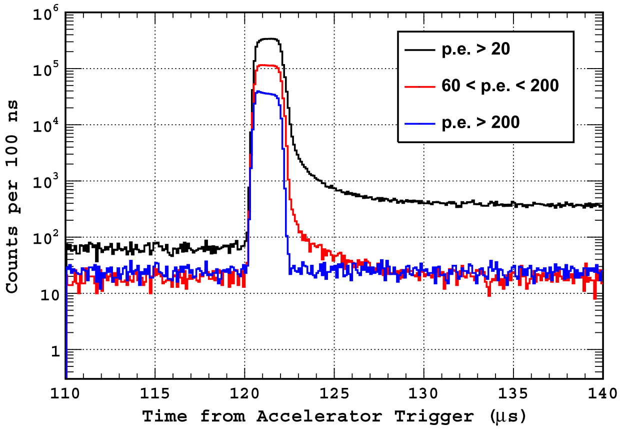

FIG. 11 (color online). The time distribution of events around the beam window for the given selection of p.e.. The dominant, black trace shows all events with p.e. > 20, the red trace selects $60 <$ p.e. < 200, and the blue trace selects p.e. > 200. The red trace can be distinguished from the blue trace because it has an excess of events above background levels immediately after the beam is off.

is consistent with high-energy neutrons losing energy in the shielding, slowing down, and arriving at delayed times. On the other hand, the blue-colored trace selecting events with p.e. > 200 does not show an appreciable excess, and its count rate returns to background levels quickly after the beam pulse. The rate immediately after the beam for the p.e. > 20 data remains significantly elevated above background levels for a longer time scale (∼200 μs). This is consistent with the 2.2 MeV, neutron-capture gamma rays from the hydrogen in mineral oil. For low event rates, neutron capture tagging can be used to discriminate primary neutrons from gamma rays, but this is not possible here because of the high event rate per beam spill. Correlating a specific neutron-capture candidate to a specific neutron primary scatter is impossible.

A minimal set of cuts is used to select events for analyzing the neutron energy spectrum and the high-energy neutron direction spectrum. A 3 μs window surrounding the beam from 120 to 123 μs after the accelerator trigger is used to select in-beam events (see Fig. 11). Also, background events are selected in a 10 ms window from 9 to 19 ms after the beam trigger and scaled for subtraction. For the neutron energy spectrum, events with p.e. > 60 are selected to minimize the gamma-ray contamination; for the direction spectrum, events with p.e. > 700 are selected to choose tracklike events.

3. Direction spectrum

The direction-spectrum for high-energy proton recoils with tracklike detector response is measured. In addition to the p.e. and timing cuts described above, events are required to be reconstructed within the inner 20% fiducial volume, and a modest set of tracklike quality cuts are made. Figure 12 shows the proton recoil direction spectrum for energetic proton recoils after cuts. Backprojecting the peak of the direction spectrum locates a possible neutron source that is approximately 10 m upstream of the BNB target. The spatial distribution of pointlike events within the SciBath detector corroborates this result. The tracking capabilities were validated against the cosmic ray muon background and muon flux from the NuMI beam during a previous deployment. When validated against the cosmic ray spectrum, our results agree with the results of Mei and Hime [55] and Miyake [56] to within 10%.

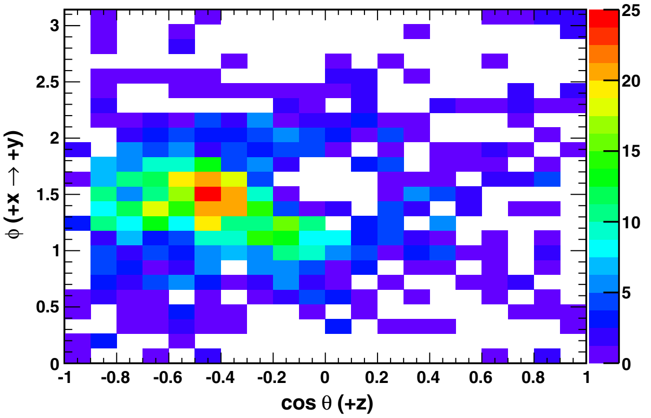

FIG. 12 (color online). Direction spectrum for high-energy proton recoils with tracklike fiber hit distribution. In our right-handed coordinate system, $+z$ is pointed towards the beam target and $+y$ is vertical. Backprojecting the peak of this distribution points in line with the beam, but about 10 m upstream of the target.

4. Neutron energy spectrum

To analyze the neutron energy spectrum, the in-beam p.e. spectrum is background subtracted for the entire data set. As shown in Fig. 13, the in-beam rate clearly dominates the background rate when scaled for the total beam exposure time of 23 s. The background-subtracted data shows a cutoff at 1600 p.e.; this is consistent with the maximum SciBath response to a single, 200 MeV proton recoil. Higher p.e. events are occasionally observed, but their origin is consistent with hadronic cascades and multiple, energetic scattering events.

The neutron energy spectrum is then unfolded from the p.e. spectrum by using the SciBath detector response as calculated with a Monte Carlo simulation. From the results of the direction spectrum, we simulated a diverging beam of neutrons with a large cross-sectional area impinging on the SciBath detector. The simulation shows that SciBath has a 0.19 m^2 effective cross-sectional area for neutron acceptance. Neutrons were uniformly generated up to 200 MeV in 20 MeV bins, and the simulation then tallied the total p.e. response for each 20 MeV neutron energy bin. The p.e. response was binned in the same way as the data,

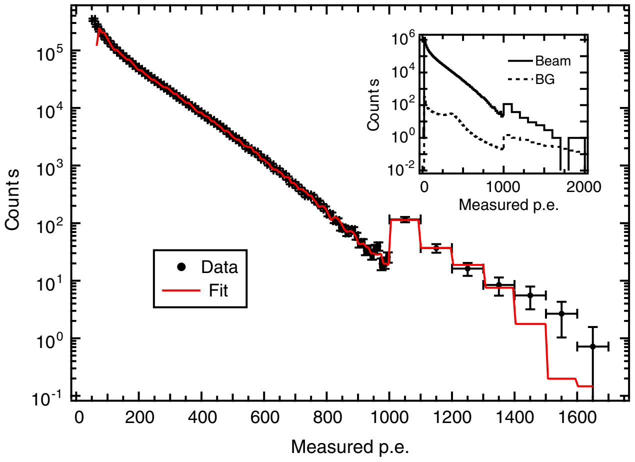

FIG. 13 (color online). The p.e. spectrum used to unfold the neutron energy spectrum. Variable width bins are used with 10 p.e. bins below 1000 p.e. and 100 p.e. bins above. The inset shows a comparison between in-beam measurements (black line) and background measurements (dashed line: 9 to 19 ms off from the beam trigger).

10 p.e. bins for p.e. < 1000 and 100 p.e. bins for p.e. ≥ 1000. A least-squares fit was performed with each 20 MeV neutron energy bin scaled by an independent fit parameter. During the fit, these fit parameters were constrained to be strictly decreasing as the neutron energy increases. These constraints were relaxed and other simulation configurations were studied in other tests of systematic uncertainties. The resulting neutron energy spectra changed very little as the constraints were relaxed.

Figure 14 shows the unfolded neutron spectrum per pulse per m^2 with the systematic uncertainties added in quadrature with the fit uncertainty. The total energy resolution is approximately 30% near the 60 p.e. threshold, and this gives an effective neutron energy threshold of approximately 10 MeV. From the unfolded neutron energy spectrum, we find the total number of neutrons above 10 MeV per pulse per m^2 is 6.3 ± 0.7. Shielding the low-energy neutron flux should not be challenging, but shielding will moderate high-energy neutrons to potentially problematic energies in the CENNS detector. With this in mind, the neutron flux above 40 MeV is particularly dangerous as a background, and we measure 2.4 ± 0.3 neutrons per pulse per m^2 above 40 MeV. Above 200 MeV, the SciBath detector loses sensitivity because recoiling protons at these energies are no longer fully contained by the detector. Fits above 200 MeV show very little significance, and the correlation matrix for the fit shows that we are unable to differentiate higher energy neutrons from 200 MeV neutrons.

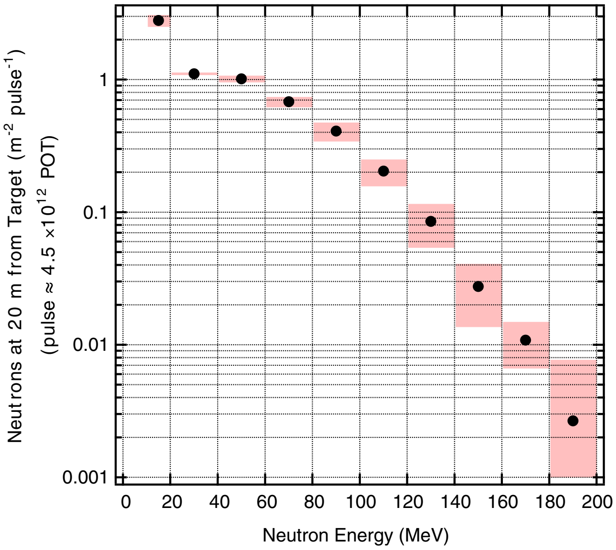

FIG. 14 (color online). The measured neutron energy spectrum by SciBath 20 m behind the proton target is shown. We measure 3.55 ± 0.38 neutrons per m^2 per beam pulse above 40 MeV, and the low-energy bin is strongly influenced by the detector threshold. The SciBath sensitivity above 200 MeV is significantly reduced, and these energy bins have large uncertainties.

5. Systematic uncertainties

In the analysis, we identified four classes of uncertainties to the neutron energy spectrum: energy scale calibration, fiducial cut, fit uncertainty, and the threshold. The dominant uncertainty above 60 MeV is due to extrapolating the energy scale calibration defined at approximately 400 p.e. (6 p.e./MeV) from cosmic ray muons to higher energies. We found that this conversion factor varied by 5% for a number of reasons: uncertainty of the muon path lengths, detector energy resolution, p.e. counting statistics, light collection efficiency as a function of position, muon input into the MC, and analysis cuts. Above the 10 MeV neutron energy threshold, the variation of the Birks' law coefficient kB had a negligible impact when compared to the other systematic uncertainties.

At low neutron energy, the choice of fiducial cut, uncertainty of the p.e. threshold, and the fit contribute roughly equally to the total uncertainty. The extraction of the neutron energy spectrum with the unfolding procedure should be independent of the choice of the central detector fiducial if the MC is correct. The neutron energy spectrum in Fig. 14 uses the entire detector, but we found very little variation, even down to 10% of the total volume. Its effect on low neutron versus high neutron energies can be understood, because attenuation at the detector edges is stronger for low-energy neutrons, whereas high-energy neutrons are more penetrating, and produce longer track proton recoils with average positions closer to the center of the detector. Because we do not have neutron-gamma discrimination at low energies, we set the p.e. threshold to 60 to remove gamma rays below 10 MeV. Due to gain shifts during the run and the extrapolation of the energy calibration to low energy, we found that a 10% variation in threshold was reasonable, and we used the MC to examine this variation on the unfolded neutron spectrum. As expected, the threshold will vary the first bin (10–20 MeV) very strongly, but has no effect above 40 MeV.

6. Cosmogenic neutron flux

For 10 ms after each beam trigger, we collected background events with a total exposure of 8.5×10^4 s. The raw p.e. spectrum is shown in Fig. 15, and the peak centered at 400 p.e. contains the minimum-ionizing, cosmic ray muons. To extract the neutron p.e. spectrum, the total p.e. plot is fit to a double exponential plus the muon response functions as calculated by the Monte Carlo. The double exponential is then fit with the same least-squares fitting procedure that was used for the in-beam data set. Gordon *et al.* [57] give a parameterization of the expected background neutron flux. For comparison, we applied our MC response function to the Gordon spectrum to generate the expected p.e. spectrum we would measure in our detector. The p.e. spectrum from Gordon was scaled by the effective area for neutron acceptance and by the total exposure time. To match the measured data, an additional

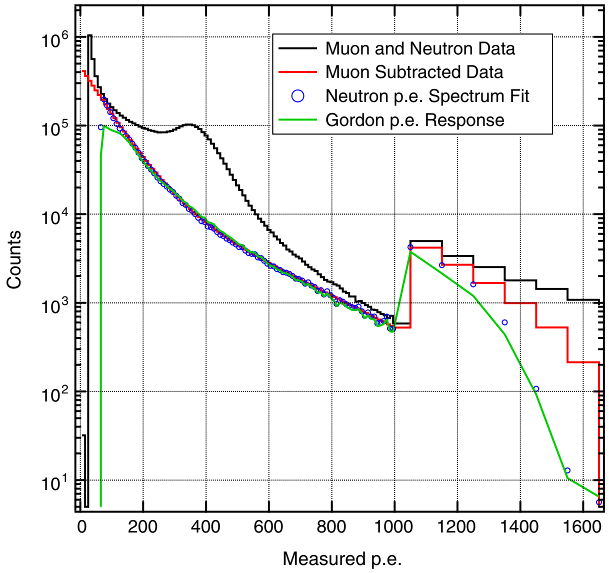

FIG. 15 (color online). Raw cosmogenic p.e. spectrum (black) with double exponential fit to neutron data (red). The unfolding process fits to the double exponential (blue markers), and the expected Gordon p.e. spectrum is also overlaid (green).

scale factor 2.4 was required. The overlaid p.e. spectra are shown in Fig. 15. Figure 16 shows the unfolded neutron energy spectrum and the expected neutron spectrum from Gordon. Aside from the factor of 2.4, our raw p.e. and unfolded neutron energy spectra shapes agree well with the parameterizations from Gordon above 20 MeV. The discrepancy between Gordon spectrum and our measurement is not unexpected because differing conditions, such as different altitudes, seasons, and air depths of these measurement, can have a strong influence on neutron fluxes. The disagreement in the lowest energy bin seems to be indicative of threshold effects. The uncertainties shown are from the fit only, but the systematic uncertainty is similar to those in the in-beam data.

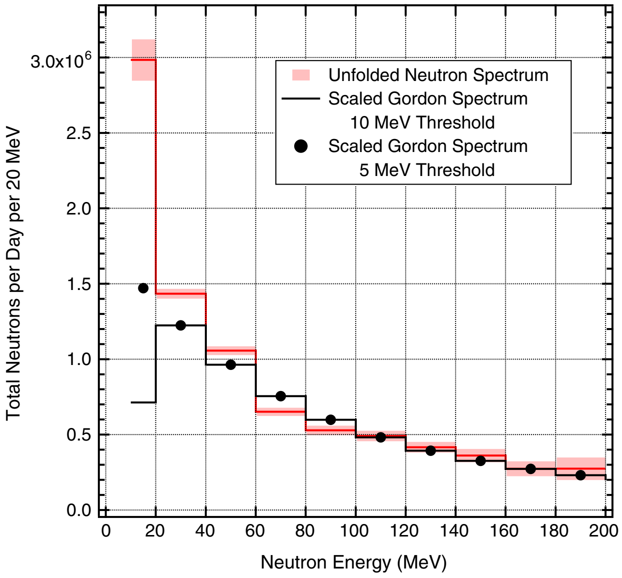

FIG. 16 (color online). The unfolded neutron spectrum (red) overlaid with the Gordon neutron spectrum with 10 MeV neutron energy threshold (black trace) and 5 MeV threshold (black) markers.

V. CENNS EXPERIMENT

A. CENNS detector

Liquid Argon (LAr) has several advantages as a detection medium. As in all of the noble liquids, LAr is naturally transparent to its own scintillation light and can be made very pure, leading to long attenuation lengths for the UV photons. Most critically, the time profile of the scintillation light created by the nuclear recoil signal is dramatically different than that for electronlike backgrounds. Radiation interacting with a noble liquid leads to the formation of dimers in the form of trapped exciton states [58]. Both singlet and triplet states are formed and create ultraviolet scintillation light at 128 nm when they decay. The lifetimes of these states are very different in LAr: 6 ns for the singlet and 1.6 μs for the triplet. Moreover, the relative amplitudes of these states depend on the type of ionizing radiation [59–61]. Boulay and Hime [62] recognized that this pulse shape discrimination allows for unprecedented rejection of ^{39}Ar beta-decay background intrinsic to the argon target, a concept that has since been demonstrated in small prototype detectors [63–65] and has led to major efforts for the direct detection of dark matter.

Of particular utility to a CENNS measurement is the so-called "single-phase" approach to dark matter detectors wherein only the primary scintillation light is recorded [62]. This approach allows one to design a detector with the high photocoverage necessary to achieve the desired light yield and low-energy threshold. The PMTs are the only active component in the detector, affording simplicity in design. Moreover, the speed for recording digital pulses is governed by the triplet lifetime of the argon scintillation light, thus avoiding difficulties with pulse pileup and dead time associated with a dual-phase time projection chamber.

The basic conceptual design of a single-phase detector is shown in Fig. 17 and is that of the CLEAR [5] and CLEAN [63] detector concepts. The key to measuring CENNS is a detector with a sufficiently large target mass (∼1000 kg) and low-energy threshold to reveal a clean nuclear-recoil signal that is free of background. The detector requirements for a CENNS measurement are similar to those for dark matter detection, however, with a key difference: Dark matter detectors need to be operated deep underground and free of cosmic ray–induced background while a CENNS detector would be placed on the surface in a neutrino beam with its associated beam-related backgrounds. A great advantage of exploiting the BNB at Fermilab comes from

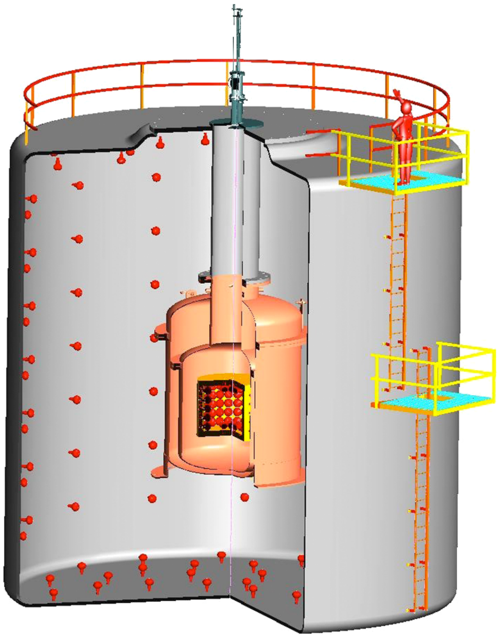

FIG. 17 (color online). Conceptual sketch of a ton-scale low-energy threshold liquid argon detector. The active volume of the inner liquid argon detector is of a ton-scale and viewed by ∼100 low-temperature phototubes with 4π coverage. The inner detector is enclosed in a vacuum insulation chamber. The outer water tank is designed for muon veto and neutron shielding.

its short-pulse time structure which provides a 5×10^{-5} duty factor against steady-state backgrounds.

By far the largest activity in the detector arises from ^{39}Ar in the LAr target. ^{39}Ar is a beta emitter ($^{39}\mathrm{Ar} \rightarrow {}^{39}\mathrm{K} + e^- + \bar{\nu}_e$, $Q = 535$ keV, $\tau_{1/2} = 269$ year). In natural argon, it is present at ∼8 parts in 10^{16}, yielding the decay rate of ∼1 Bq/kg. The unique attack on this intrinsic background is PSD. As can be seen in Fig. 18, the ability to reject the internal ^{39}Ar background is a very strong function of the light yield, which in turn dictates what can be achieved as an analysis energy threshold. Leakage is defined as the fraction of background events that are mistaken as nuclear recoil events in an acceptance window of 50% using a simple statistic comparing the prompt-to-late light ratio [62,63]. The model for leakage has been developed in detail for the MiniCLEAN detector using constraints from data obtained in prototype experiments [64,66] and including details of scintillation light production, propagation, reemission from the WLS and detection in the PMT array with measured single p.e. response and noise. The pulsed structure of the BNB provides significant reduction in this background. Most relevant, the limits set on background leakage from the DEAP-1 experiment [66] of three parts in 10^8 already surpass the requirements of a CENNS measurement. If, for example, we assume 6 p.e./keV$_{ee}$ for light yield, then one can expect to achieve an energy threshold of 10 keV$_{ee}$ (40 keV$_{nr}$) with leakage of only one ^{39}Ar event in an exposure of 1 ton-year.

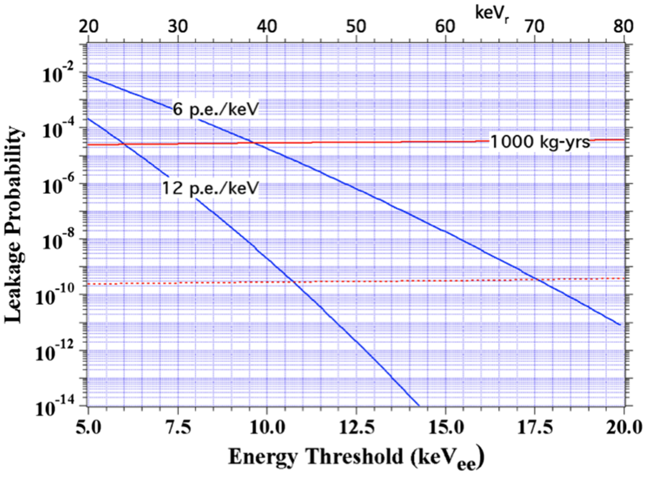

FIG. 18 (color online). Leakage probability of the ^{39}Ar background as a function of energy threshold. The dotted red line indicates the statistical leakage rate of ^{39}Ar events into the signal region for 1 ton-year detector livetime. The solid red line indicates the leakage rate tolerable after duty factor correction (5×10^{-5}). Solid blue curves show the impact of PSD cuts in the leakage probability for two different light yield assumptions. See text for details.

The assumption of 6 p.e./keV$_{ee}$ is based on that measured in MicroCLEAN [62] and projected for MiniCLEAN [63] using the Hamamatsu R5912-02MOD PMTs submerged and operating cold in LAr.

Significant improvements are foreseen with PMT technologies that increase the efficiency of 19% for the R5912-02MOD to ∼32%. Simplification and optimization of the optical light guides designed for MiniCLEAN could also improve light yield by as much as 30% [67]; hence, it is quite reasonable to consider a single-phase LAr detector with light yield as high as 12 p.e./keV$_{ee}$. As can be seen in Table I, this would yield a detector with an energy threshold as low as 6 keV$_{ee}$ (24 keV$_{nr}$) that is essentially free of steady-state and detector-related background.

In addition to ^{39}Ar in the sensitive volume, there are external backgrounds arising from the detector construction materials themselves. Table II contains a projection of the non-^{39}Ar backgrounds after scaling the MiniCLEAN backgrounds to a 1-ton detector target and appropriate surface area [63]. Unlike a dark matter detector, the CENNS detector can employ the full target mass without fiducialization since the duty factor of the BNB is such as to make the steady backgrounds from neutrons and surface radon progeny negligible. Therefore, a CENNS experiment does not require this extreme level of radon background control. Hence, we assume 100 decays/m^2/day or lower of modest level radon daughter decay rate in the energy region of interest, which is reasonably achievable [66].

Figure 19 shows the event rate of CENNS in a 1-ton liquid argon neutrino detector given a neutrino flux of 5×10^5 ν/cm^2/s when the detector is located 20 m away

TABLE I. CENNS signal and ^{39}Ar background (events/year) for a 1-ton detector assuming 50% acceptance in rejecting electron and gamma background. The background rate is determined for the energy window between energy threshold and 100 keV$_{nr}$ (25 keV$_{ee}$).

Energy Threshold		Background			
(keV$_{ee}$/keV$_{nr}$)	Signal	6 p.e./keV$_{ee}$	8 p.e./keV$_{ee}$	10 p.e./keV$_{ee}$	12 p.e./keV$_{ee}$
5/20	320	228	69	21.6	6.8
7.5/30	196	11.5	1.5	0.21	0.03
10/40	136	0.45	0.02	0.001	…

TABLE II. Backgrounds in the 1-ton CENNS detector arising from (α,n) neutrons from the PMTs and steel. The radon background is from Tetraphenyl butadiene and acrylic.

Source	Production Rate (/ton/year)	Detection Rate (events/ton/year)	E < 25 keV$_{ee}$	$12.5 <$ E < 25 keV$_{ee}$
PMT(α, n)	66,700	11,340	1520	710
Steel(α, n)	3680	495	65	30
Total(α, n)	70,380	11,835	1585	740
Total(α, n) × duty factor	3.5	0.6	0.08	0.04
Radon	15,880		7,147 ($25 <$ E < 100 keV$_{nr}$)	
Radon × duty factor	0.8		0.36	

from the target at a far off-axis site. Assuming a flat ~50% detection efficiency, which is mostly from the PSD cut efficiency [64,65], we expect about ~250 CENNS events/ton/year at 25 keV$_{nr}$ energy threshold after background subtraction (at 32 kW beam power). The beam-induced neutron backgrounds and systematic uncertainties are discussed in the following sections.

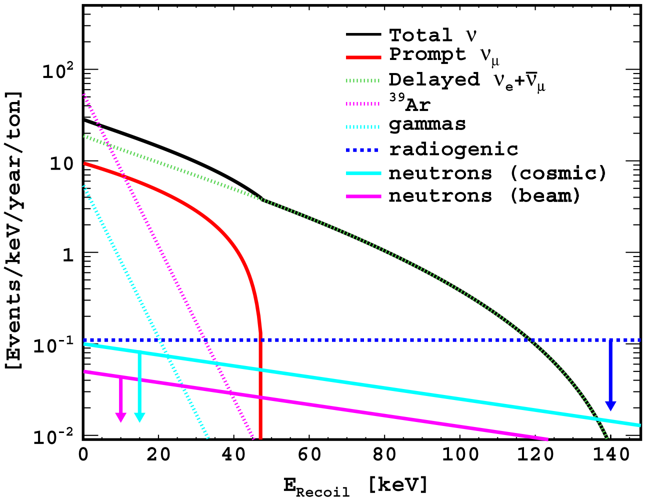

FIG. 19 (color online). Number of expected CENNS events with the far off-axis BNB (32 kW) neutrino flux. The liquid argon detector is assumed to be located 20 m away from the target. The beam-induced (cosmogenic) neutron background estimate is based on the SciBath measurement. It assumes 7 m (4 m) of concrete shielding but without the water shield (see Fig. 20). A flat 50% detection efficiency is applied to the nuclear recoil events.

B. Neutron shielding

The measured, beam-induced neutrons (see Fig. 14) can be significantly reduced with proper shielding. The fast neutron component above 100 MeV requires special attention in the shielding design. These neutrons may slow down in the shielding material itself and then become a more difficult background component with slower neutrons of less than a few MeV energy. We carried out a Monte Carlo N-Particle eXtended (MCNPX) and Geant-4 based Monte Carlo simulations in order to evaluate the overall level of neutron shielding that is needed for a CENNS experiment. We used the measured, beam-induced neutron fluxes as input to the simulation. We found these neutron fluxes can be substantially suppressed by more than 7 orders of magnitude after 7 m of concrete shielding. Figure 20 shows the results of the Geant-4 MC simulation. MCNPX results are consistent with the Geant-4 results. We also found that measured cosmogenic neutrons can be significantly suppressed with 4 m of concrete shielding. Given these levels of concrete shielding, the total number of neutrons that enter the detector's water shielding within the detector livetime can be less than 20 per m^2 per year of operation time.

The neutrons entering the water shielding (10 m in diameter) are then passed to the liquid argon detector in the Geant-4 MC. In order to boost the statistical sensitivity of the neutrons, we simulated one million neutrons and then scaled them to the expected input neutron fluxes. The resulting neutron-nucleus event rate in the liquid argon detector with water shielding is negligible (less than 10^{-3} events/ton/year). To understand the effect of our shielding options, Fig. 19 shows the neutron-nuclear recoil

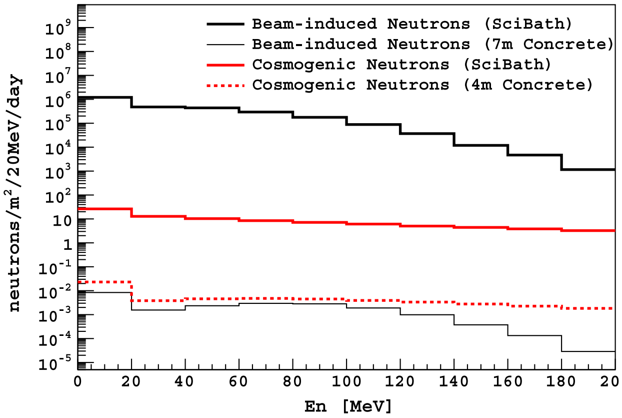

FIG. 20 (color online). Neutron flux reduction with concrete shielding. The thick black solid line is beam-induced neutrons and the thick red solid line is cosmogenic neutrons measured by SciBath detector. The detector livetime corrections are made for both input neutron fluxes. The thin black line is beam-induced neutron flux after passing 7 m of concrete shielding. The dotted red line is cosmogenic neutron flux after passing 4 m of concrete shielding.

events (without water shielding) after 7 m of concrete for the beam-induced neutron flux and 4 m of concrete for the cosmogenic neutron flux. To be conservative, the neutron background events include not only single scattering events but also multiple scattering nuclear recoil events in the LAr fiducial volume. The expected number of background events is only 1.4 events for beam-induced neutrons and 2.5 events for cosmogenic neutrons within the energy region of interest (25 keV_{nr} to 100 keV_{nr}). This low-background configuration suggests that the CENNS detector can be placed as close as 14 m away from the target where we expect twice the neutrino flux compared to the 20 m location. However, it is also true that predicting the neutron flux through a massive shield without an accurate understanding of shielding configurations is quite challenging. Therefore, beam tests of various neutron shielding configuration would be needed. One important check is to see if the neutrons are from "sky shine," directly from the target, or from the beam line. The water veto in Fig. 17 is designed to shield out unexpected neutron leakages from the massive concrete shielding. The large water tank configuration will allow us to easily reconfigure the shielding level by relocating the LAr detector in the tank.

C. Systematics and sensitivity of experiment

There are two major sources of systematic uncertainties in a CENNS experiment: (1) uncertainties of stopping pion production at the target, and hence the related systematic uncertainties of the absolute flux of neutrinos at the far-off-axis, and (2) uncertainties of scintillation yield (*Leff*) in a LAr detector for the measurement of low-energy nuclear-recoil events. The other sources of systematics—such as beam-induced neutron backgrounds, cosmogenic neutrons, gamma backgrounds, ambient radioactive decays, and uncertainties from high-energy neutrino interactions near or in the detector—depend on the specific experimental design or are minor background contributions.

1. Uncertainty of neutrino flux

The uncertainty in neutrino production from stopped pions and muons is dominated by the uncertainty of the pion production in the BNB target and surrounding materials. The HARP experiment at CERN measured pion production from both thin beryllium targets and a replica BNB target at the 8 GeV proton energy that the BNB uses. The uncertainty of the pion production measured by HARP was 7% [68,69]. In addition to the uncertainty in direct pion production, there are uncertainties that arise from the secondary production of pions and uncertainties in the fraction of pions and muons that get to decay rather than interact. These additional uncertainties are estimated to be at the 5% level [44]. This gives a total of 9% neutrino flux uncertainty.

2. Uncertainties from Leff of liquid argon detector

The scintillation efficiency for nuclear recoils relative to the electron-equivalent efficiency, referred to as *Leff*, has been measured for LAr in MicroCLEAN [70] and independently by Regenfus *et al.* [71] as $0.25 \pm 0.01 \pm 0.01$ and 0.29 ± 0.03, respectively. The data, shown in Fig. 21, are in good agreement with a model that combines simple Lindhard theory with Birks' saturation law [73]. The scintillation efficiency for nuclear recoils is essentially flat, independent of energy, for recoil energies above

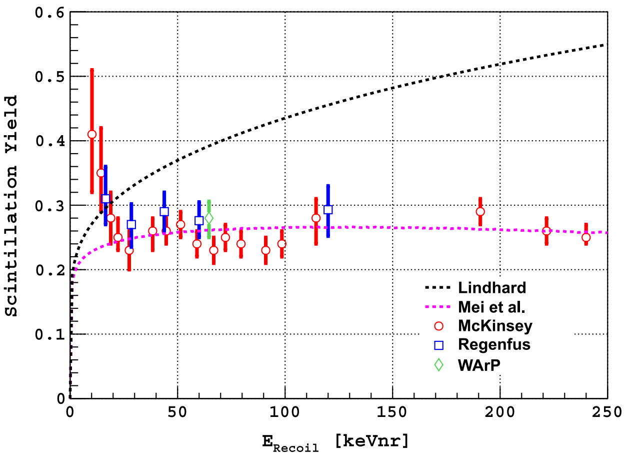

FIG. 21 (color online). The scintillation efficiency for nuclear recoils relative to the electron equivalent measured in MicroCLEAN (red circle [64]), Regenfus *et al.* (blue square [71]) and the single averaged value from WArP (green diamond [72]). The model of Mei *et al.* [73] combines the Lindhard theory with Birks' saturation, providing the phenomenological description indicated.

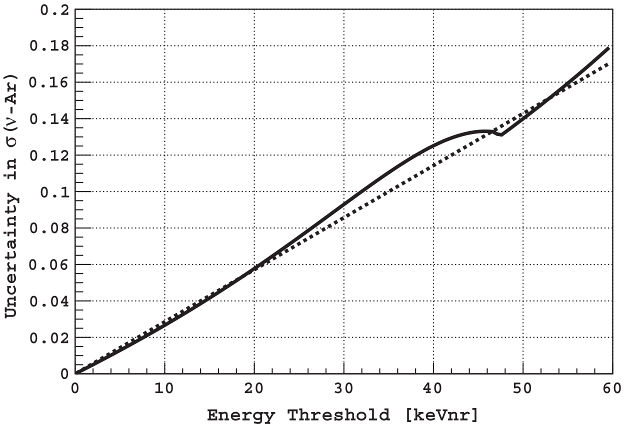

FIG. 22. Extracted cross section uncertainty as a function of energy threshold due to the intrinsic uncertainty in *Leff* of 6.5%. The dashed curve indicates the uncertainty calculated using an analytical approximation to the shape of the differential neutrino-nucleus scattering spectrum, and the solid curve uses the true spectrum as simulated for the BNB. The uncertainty in *Leff* effectively induces an uncertainty in knowledge of the energy threshold, and thus the integrated event rate above or below that threshold. The bump structure near ~47 keV_{nr} comes from the similar structure in the event rate at the same energy (see Fig. 19, black curve) as the *Leff* is changing monotonically in these energies.

~20 keV_{nr}. The combined measurements provide $Leff = 0.262 \pm 0.017$. A possible upturn in *Leff* at the lowest energies measured is interesting and worth further exploration. Measurements are typically made of the nuclear recoil scintillation yield relative to a calibrated energy scale for gammas, and it is usually assumed that the scintillation yield for gammas is independent of energy. Figure 22 shows expected cross section uncertainty as a function of energy threshold due to the *Leff*. At the energy threshold of 25 keV_{nr} the measurement uncertainty of cross section by *Leff* is 7.5%.

3. Uncertainties from high-energy neutrino interactions

The high-energy neutrinos [> 55 MeV, see Fig. 6(b)] are produced by muon capture and kaon decay at rest. These neutrinos represent only 3% of the total neutrino fluxes. However, these high-energy neutrinos may produce two types of background events: (1) direct neutrino interactions in the liquid argon volume, and (2) neutrino interactions in the water shield which result in secondary neutrons reaching the sensitive detector volume and leaving nuclear recoils in the signal region.

We carried out a detector simulation for high-energy neutrino interactions using FLUKA [74–76]. The neutrino interactions were weighted by the neutrino-nucleus cross sections obtained with the GENIE(2.8.0) [77] neutrino simulation package. Table III shows the above two background cases.

TABLE III. Expected background events by $E_\nu > 55$ MeV which deposit energy of 25 to 100 keV per ton liquid argon detector per year. The numbers of events with secondaries produced in (or reaching) the sensitive volume are presented in the "all events" columns. More critical events containing one or more neutrons are given by the "$w/$neutrons" columns.

	Liquid argon		Water shield	
	All events	w/neutrons	All events	w/neutrons
ν_e	0.00	0.00	0.00	0.00
ν_μ	0.39	0.28	1.04	0.12
$\bar{\nu}_\mu$	0.04	0.02	0.01	0.00
Sum	0.43	**0.30**	1.05	**0.12**

The CENNS signal is identified by single nuclear recoils in the energy range 25 keV to 100 keV, and the most serious background is expected from nuclear recoils caused by undetected neutron scattering. An upper limit of 0.42 events (= 0.30 + 0.12 events or 0.21 events after applying 50% detection efficiency) per ton-year is found for the neutrino-induced background. Because the number of expected background events is small, statistical uncertainties in the simulation are not expected to be relevant. The largest systematic uncertainty of this study arises from the neutrino-argon cross section uncertainties in the GENIE model in the relevant neutrino energy range (55 to 250 MeV), which has never been measured. However, even if we assume an order of magnitude of uncertainty in the GENIE cross section model in this energy region, the backgrounds by the high-energy neutrinos are expected to be about 1% of the total number of CENNS signal events.

4. Uncertainties from beam-induced neutrons

The neutron flux measurement by SciBath and results from a neutron shielding MC study indicate that the beam-induced neutrons can be substantially reduced with proper shielding design and could have a negligible impact on the CENNS event rates. However, due to the potential unknowns of these fast-neutron shielding effects, and our current uncertainty in neutron sources and directions, we

TABLE IV. Systematic uncertainties of the event rate of CENNS experiment. The detector energy threshold is assumed to be $E_{th} \geq 25$ keV_{nr}.

	Uncertainty
Neutrino flux	9%
Leff of LAr	7.5%
High-energy neutrinos	< 1%
Beam-induced neutrons	< 1%
Cosmogenic neutrons	< 1%
^{39}Ar and gammas	< 1%
Radiogenic backgrounds	< 1%
Total uncertainty	**12%**

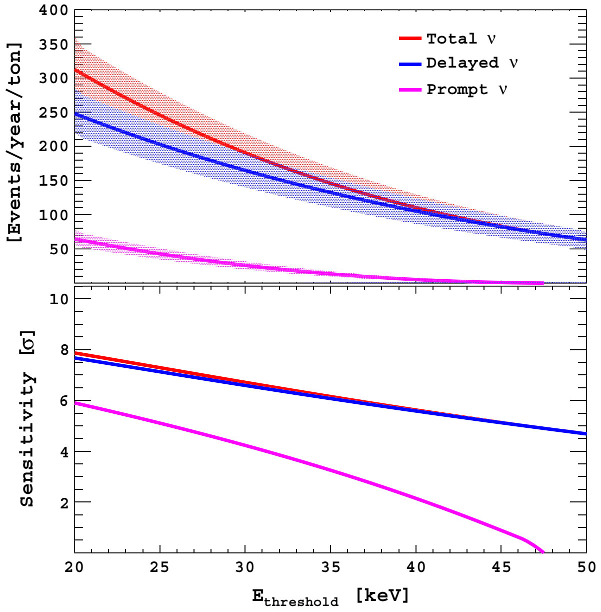

FIG. 23 (color online). Sensitivity of CENNS measurement. The integrated signal event rates per ton after one-year operation as a function of detector energy threshold (top plot), and the sensitivity of CENNS measurement in σ (bottom plot). A flat detection efficiency of 50% over the energy range is assumed. The error bands on the top plot are 1 sigma quadratic-sum errors of statistical and systematic errors ($\sigma^2 = \sigma^2_{stat} + \sigma^2_{syst}$). We used Table IV values for the systematic errors, except for the ^{39}Ar and gamma backgrounds systematics which are from Fig. 19, and the *Leff* systematics for which we used the function from Fig. 22.

assign a systematic uncertainty of beam-induced neutrons on the CENNS event rate at the 1% level.

5. Uncertainties from cosmogenic neutrons, gammas, radons and ^{39}Ar

The non-beam-related backgrounds can be significantly suppressed by the duty factor. Therefore, the background requirement of the CENNS experiment is far less stringent than that of typical dark matter or other low background experiments. Cosmic ray backgrounds can be further reduced by an active veto system in the water shielding, or it can also be significantly suppressed by 4 m of passive concrete shielding (see Fig. 20). The expected systematic uncertainty of the cosmogenic neutron events in the signal rate is less than 1%. The gamma backgrounds are produced mostly by the decay chain of ^{238}U, ^{232}Th, and ^{40}K in the PMT glass windows. These gamma backgrounds can also be suppressed by the duty factor, PSD, and fiducial volume cuts. As shown in Fig. 19, the contribution of the gamma backgrounds in the signal region is negligible. The backgrounds from the radon daughters, especially ^{210}Po, can produce nuclear recoils in the signal region. The radon daughter backgrounds in the signal region are expected to be negligible after the pulse timing cut. Moreover, the steady-state backgrounds can be separately measured by the beam-off data in the energy region of interest and can be subtracted from the signal shape. Therefore, the systematic uncertainty due to radioactive backgrounds is conservatively assumed to be less than 1%.

Table IV summarizes the systematic uncertainties. The total systematic uncertainty in event rate is expected to be 12%. Figure 23 shows sensitivity of the CENNS measurement as a function of detector energy threshold with 1 ton-year exposure at 20 m from the BNB target. A 7.5 sigma measurement of the CENNS is expected at the detector energy threshold of 25 keV$_{nr}$.

VI. SUMMARY

In this report, we have presented a unique experimental method for measuring the coherent elastic neutrino-nucleus scattering, utilizing low-energy neutrinos emitted at the far off-axis of a high-energy neutrino beam. To determine the feasibility of this approach, we have made neutron background measurements at the Fermilab Booster Neutrino Beam. Our results indicate that this method can result in a successful experiment. With the BNB neutrino source, non-beam-related backgrounds such as cosmic rays and internal and external radioactivity are substantially suppressed by the beam duty factor. The measured beam-induced neutron backgrounds can be safely reduced with proper shielding. We show that a one-ton fiducial mass single-phase liquid argon detector can make a 7.5 sigma discovery of CENNS at the detector energy threshold of 25 keV$_{nr}$. Further development of a low-energy neutrino source at Fermilab as part of programs like Project-X [78] and nuSTORM [79] will provide excellent resources for future low-energy neutrino physics experiments.

ACKNOWLEDGMENTS

The authors are grateful to R. Davis, W. Jaskierny, W. Miner, K. Taheri and J. Volk for providing technical and engineering help with the neutron flux measurement at the Fermilab Booster target building. We would also like to acknowledge H. O. Meyer for crucial work on the SciBath concept and detector construction. This work is supported by the Department of Energy, Fermilab University Research Association Visiting Scholar program, NSF-1068712, NSF-1306942 and NSF-1005233.

[1] D. Z. Freedman, Phys. Rev. D **9**, 1389 (1974).
[2] J. Yoo, Contribution for the Short-Baseline Neutrino Workshop (2011), Fermilab, IL, USA, https://indico.fnal.gov/conferenceDisplay.py?confId=4157.
[3] H. T. Wong, H.-B. Li, J. Li, Q. Yue, and Z.-Y. Zhou, J. Phys. Conf. Ser. **39**, 266 (2006).
[4] P. Barbeau, J. Collar, and O. Tench, J. Cosmol. Astropart. Phys. 09, (2007) 009.
[5] K. Scholberg *et al.*, arXiv:0910.1989.
[6] D. Akimov *et al.* (CSI Collaboration), arXiv:1310.0125.
[7] G. Jungman, M. Kamionkowski, and K. Griest, Phys. Rep. **267**, 195 (1996).
[8] S. Arrenberg, L. Baudis, K. Kong, K. T. Matchev, and J. Yoo, Phys. Rev. D **78**, 056002 (2008).
[9] J. Monroe and P. Fisher, Phys. Rev. D **76**, 033007 (2007).
[10] L. E. Strigari, New J. Phys. **11**, 105011 (2009).
[11] J. Billard, L. Strigari, and E. Figueroa-Feliciano, Phys. Rev. D **89**, 023524 (2014).
[12] P. Cushman *et al.*, arXiv:1310.8327.
[13] D. Z. Freedman, D. N. Schramm, and D. L. Tubbs, Annu. Rev. Nucl. Sci. **27**, 167 (1977).
[14] D. McKinsey and J. Doyle, J. Low Temp. Phys. **118**, 153 (2000).
[15] D. N. McKinsey and K. Coakley, Astropart. Phys. **22**, 355 (2005).
[16] J. A. Nikkel, R. Hasty, W. H. Lippincott, and D. N. McKinsey, Astropart. Phys. **29**, 161 (2008).
[17] C. J. Horowitz, K. Coakley, and D. McKinsey, Phys. Rev. D **68**, 023005 (2003).
[18] K. Scholberg, Annu. Rev. Nucl. Part. Sci. **62**, 81 (2012).
[19] S. Chakraborty, P. Bhattacharjee, and K. Kar, Phys. Rev. D **89**, 013011 (2014).
[20] A. Aguilar-Arevalo *et al.* (LSND Collaboration), Phys. Rev. D **64**, 112007 (2001).
[21] A. Aguilar-Arevalo *et al.* (MiniBooNE Collaboration), Phys. Rev. Lett. **110**, 161801 (2013).
[22] G. Garvey, A. Green, C. Green, W. Louis, G. Mills, G. McGregor, H. Ray, R. Schirato, R. Van de Water, and D. White, Phys. Rev. D **72**, 092001 (2005).
[23] A. J. Anderson, J. M. Conrad, E. Figueroa-Feliciano, C. Ignarra, G. Karagiorgi, K. Scholberg, M. H. Shaevitz, and J. Spitz, Phys. Rev. D **86**, 013004 (2012).
[24] P. Vogel and J. Engel, Phys. Rev. D **39**, 3378 (1989).
[25] N. F. Bell, M. Gorchtein, M. J. Ramsey-Musolf, P. Vogel, and P. Wang, Phys. Lett. B **642**, 377 (2006).
[26] A. G. Beda, V. B. Brudanin, V. G. Egorov, D. V. Medvedev, M. V. Shirchenko, and A. S. Starostin, Phys. Part. Nucl. Lett. **7**, 406 (2010).
[27] L. B. Auerbach *et al.* (LSND Collaboration), Phys. Rev. D **63**, 112001 (2001).
[28] G. G. Raffelt, Phys. Rev. Lett. **64**, 2856 (1990).
[29] A. Ayala, J. C. D'Olivo, and M. Torres, Phys. Rev. D **59**, 111901 (1999).
[30] J. Barranco, O. G. Miranda, and T. I. Rashba, J. High Energy Phys. 12 (2005) 021.
[31] S. Davidson, C. Pena-Garay, N. Rius, and A. Santamaria, J. High Energy Phys. 03 (2003) 011.
[32] K. Scholberg, Phys. Rev. D **73**, 033005 (2006).
[33] J. Barranco, O. G. Miranda, and T. I. Rashba, Phys. Rev. D **76**, 073008 (2007).
[34] J. Dorenbosch *et al.* (CHARM Collaboration), Phys. Lett. B **180**, 303 (1986).
[35] A. Steiner, M. Prakash, J. Lattimer, and P. Ellis, Phys. Rep. **411**, 325 (2005).
[36] K. Patton, J. Engel, G. C. McLaughlin, and N. Schunck, Phys. Rev. C **86**, 024612 (2012).
[37] P. Amanik and G. McLaughlin, J. Phys. G **36**, 015105 (2009).
[38] C. Horowitz and J. Piekarewicz, Phys. Rev. Lett. **86**, 5647 (2001).
[39] M. Elnimr *et al.* (OscSNS Collaboration), arXiv:1307.7097.
[40] Y. Efremenko and W. Hix, J. Phys. Conf. Ser. **173**, 012006 (2009).
[41] A. Bolozdynya *et al.*, arXiv:1211.5199.
[42] Figure is taken from a MiniBooNE site plan, Drawing No. 6-7-52 CDR-2 (1999).
[43] R. Stefanski *et al.*, Fermilab internal report, Project 6-7-55, 2000.
[44] A. A. Aguilar-Arevalo *et al.* (MiniBooNE Collaboration), Phys. Rev. D **79**, 072002 (2009).
[45] I. Stancu, Fermilab internal report, 2001.
[46] R. Tayloe, H. O. Meyer, D. C. Cox, J. Doskow, A. Ferguson, T. Katori, M. Novak, and D. Passmore, Nucl. Instrum. Methods Phys. Res., Sect. A **562**, 198 (2006).
[47] R. Cooper *et al.*, arXiv:1110.4432.
[48] V. V. Verbinski, W. R. Burrus, T. A. Love, W. Zobel, N. W. Hill, and R. Textor, Nucl. Instrum. Methods **65**, 8 (1968).
[49] J. M. Adams and G. White, Nucl. Instrum. Methods **156**, 459 (1978).
[50] R. A. Cecil, B. D. Anderson, and R. Madey, Nucl. Instrum. Methods **161**, 439 (1979).
[51] L. Bugel *et al.* (FINeSSE Collaboration), arXiv:hep-ex/0402007.
[52] Eljen Technology, Sweetwater, TX, www.eljentechnology.com, accessed Mar. 5, 2013.
[53] Saint-Gobain Crystals, http://www.detectors.saint-gobain.com, accessed Mar. 5, 2013.
[54] B. Braizinha, J. Esterline, H. Karwowski, and W. Tornow, Nucl. Instrum. Methods Phys. Res., Sect. A **623**, 1046 (2010).
[55] D. Mei and A. Hime, Phys. Rev. D **73**, 053004 (2006).
[56] S. Miyake, in *13th International Cosmic Ray Conference, University of Denver, Denver Colorado, USA, 17-30 August 1973,* Vol. 5, (University of Denver, Denver, 1973) p. 3638.
[57] M. S. Gordon, P. Goldhagen, K. P. Rodbell, T. H. Zabel, H. H. K. Tang, J. M. Clem, and P. Bailey, IEEE Trans. Nucl. Sci. **51**, 3427 (2004).
[58] S. Kubota, A. Nakamoto, T. Takahashi, S. Konno, T. Hamada, M. Miyajima, A. Hitachi, E. Shibamura, and T. Doke, Phys. Rev. B **13**, 1649 (1976).
[59] A. Hitachi, T. Takahashi, N. Funayama, K. Masuda, J. Kikuchi, and T. Doke, Phys. Rev. B **27**, 5279 (1983).
[60] T. Doke, H. J. Crawford, A. Hitachi, J. Kikuchi, P. J. Lindstrom, K. Masuda, E. Shibamura, and T. Takahashi, Nucl. Instrum. Methods Phys. Res., Sect. A **269**, 291 (1988).
[61] T. Doke, A. Hitachi, J. Kikuchi, K. Masuda, H. Okada, and E. Shibamura, Jpn. J. Appl. Phys. **41**, 1538 (2002).
[62] M. G. Boulay and A. Hime, Astropart. Phys. **25**, 179 (2006).
[63] A. Hime (MiniCLEAN Collaboration), arXiv:1110.1005.
[64] W. Lippincott, K. Coakley, D. Gastler, A. Hime, E. Kearns, D. McKinsey, J. Nikkel, and L. Stonehill, Phys. Rev. C **78**, 035801 (2008).

[65] P. Benetti *et al.*, Astropart. Phys. **28**, 495 (2008).

[66] M. Boulay *et al.*, arXiv:0904.2930.

[67] T. Alexander *et al.*, Astropart. Phys. **49**, 44 (2013).

[68] M. Catanesi *et al.* (HARP Collaboration), Eur. Phys. J. C **52**, 29 (2007).

[69] D. W. Schmitz, Ph.D. thesis, Columbia University, 2008.

[70] D. Gastler, E. Kearns, A. Hime, L. C. Stonehill, S. Seibert, J. Klein, W. Hugh Lippincott, D. N. McKinsey, and J. A. Nikkel, Phys. Rev. C **85**, 065811 (2012).

[71] C. Regenfus, in *IDM2006 Proceedings* (World Scientific, Singapore, 2006), p. 325.

[72] R. Brunetti *et al.* (WArP Collaboration), New Astron. Rev. **49**, 265 (2005).

[73] D.-M. Mei, Z.-B. Yin, L. Stonehill, and A. Hime, Astropart. Phys. **30**, 12 (2008).

[74] G. Battistoni, F. Cerutti, A. Fassò, A. Ferrari, S. Muraro, J. Ranft, S. Roesler, and P. R. Sala, AIP Conf. Proc. **896**, 31 (2007).

[75] A. Ferrari, P. R Sala, A. Fassò, and J. Ranft, Report Nos. CERN-2005-010, SLAC-R-773, INFN-TC-05-11, 2005.

[76] *Proceedings of 12th International Conference on Nuclear Reaction Mechanisms, Villa Monastero, Verenna, Italy, 2009*, edited by C. Francesco and A. Ferrari (CERN, Geneva, Switzerland, 2010).

[77] C. Andreopoulos *et al.*, Nucl. Instrum. Methods Phys. Res., Sect. A **614**, 87 (2010).

[78] A. S. Kronfeld *et al.*, arXiv:1306.5009.

[79] D. Adey *et al.* (nuSTORM Collaboration), arXiv:1308.6822.